University of Seville

Master in Nuclear Physics 2016/2017

Impact of externally applied 3D fields on plasma rotation and correlation to particle losses

Pilar Cano Megías

Supervisor:
Eleonora Viezzer

Departamento de Física Atómica, Molecular y Nuclear
Facultad de Física

Plasma Science and Fusion Technology
Centro Nacional de Aceleradores

Resumen

El modo de alto confinamiento (H-mode) está considerado como el modo de operación óptimo para futuros dispositivos de fusión nuclear. El H-mode viene acompañado de inestabilidades que provocan la expulsión de partículas y energía, y deterioran el confinamiento del plasma. Aunque dichas inestabilidades son tolerables en los dispositivos actuales, el desarrollo de técnicas para su control es fundamental de cara a garantizar la integridad de futuros reactores.

La aplicación de perturbaciones magnéticas externas es una de las herramientas más extendidas para la mitigación e incluso completa supresión de dichas inestabilidades. Estas perturbaciones alteran la simetría del campo magnético que confina al plasma. La respuesta del plasma a dichas perturbaciones es una línea de investigación muy activa actualmente.

El objetivo de este trabajo es el estudio detallado de dos descargas de baja colisionalidad, llevadas a cabo en el tokamak ASDEX Upgrade. Durante estas descargas se aplican perturbaciones magnéticas externas para estudiar la respuesta del plasma. El estudio está centrado en el análisis de la evolución temporal acoplada de la rotación toroidal de las impurezas, pérdida de iones rápidos y densidad. Los resultados obtenidos revelan fuertes correlaciones entre estos parámetros. Las interdependencias entre las magnitudes dependen de (1) la caracterización de la población de iones rápidos sujeta a pérdidas y (2) la posición radial en la que se miden rotación y densidad. Se han observado fuertes cambios en el patrón de correlaciones asociados a las diferencias en las órbitas de los iones rápidos; y la intensificación de la correlación hacia el borde del plasma. Bajo determinadas circunstancias, se produce un cambio en el sentido de giro de la rotación toroidal de las impurezas en el borde del plasma, i.e. las impurezas en el borde y en el centro giran en sentido contrario. Ello también conlleva un cambio en el patrón de la correlación.

Abstract

The high-confinement mode (H-mode) is considered to be the baseline operational scenario for future nuclear fusion devices. The H-mode is accompanied by instabilities that cause cyclic ejection of particles and energy, thus deteriorating the confinement of the plasma. Although these instabilities are tolerable in current experiments, the development of techniques for their control is crucial to guarantee the integrity of future devices.

The application of external 3D magnetic fields is one of the most efficient techniques to achieve the mitigation and even full suppression of these instabilities. These magnetic perturbations break the symmetry of the magnetic field. The impact of the perturbations on the plasma is currently a very active research line.

The objective of this thesis is a detailed analysis of two low collisionality discharges, which were carried out in the ASDEX Upgrade tokamak experiment. In these two discharges static magnetic perturbations were applied to study plasma response. The study is focused on the observation of the coupled evolution of the toroidal impurity rotation, fast-ion losses and electron density. The results reveal strong correlations between the parameters. The interdependencies between the parameters depend on (1) the type of fast-ion population which is subject to losses and (2) the radial position at which rotation and density are measured. A strong change in the correlation pattern is associated with changes in the orbit topology of the fast-ions. The correlation towards the plasma edge becomes more intense. Under certain circumstances, a change in the correlation pattern at the edge is connected to an impurity toroidal rotation reversal, i.e. a spin-up of the impurities in opposite direction to the plasma core.

Contents

Chapter 1

Introduction

1.1 Fusion energy

The worldwide increasing population and energy consumption requires mankind to meet the challenge of searching for new energy sources, besides the necessity of reducing environmental impact (i.e., greenhouse gases emissions and consequent global warming) that current main energy production processes imply. Fusion energy provides a promising possibility for future civilizations. Among its main remarkable features are:

- **High energy production/consumed fuel ratio**: The amount of energy released in nuclear reactions is up to six orders of magnitude higher than in chemical reactions (i.e. fossil fuels combustion) per unit of mass of fuel consumed. This is because the production of energy relies on the strong interaction and the energy gain the rearrangement of the nuclei.

- **Virtually unlimited fuel resources**. In fusion reactions, two light nuclei fuse to produce a heavier one. In thermonuclear fusion, deuterium (D) and tritium (T) are the reactants. D is present in 0.015% of sea water molecules. T is expected to be produced from lithium (which is abundant and uniformly distributed in Earth's crust and ocean waters) in future nuclear fusion power plants. This means D reserves can meet current demand levels for 20 billions of years while T reserves are sufficient for the next 300.000 years.

- **CO_2 emission-free**. Fusion energy will contribute to the clean energy production share, helping environment preservation and pollution reduction.

– **Climate independence**. It makes fusion energy very appropriate for covering base load energy demand and constitutes an advantage when comparing with renewable energies (e.g. solar and wind energy strongly depend on weather and climate patterns).

1.2 Fusion reaction

Differences in the binding energy per nucleon allow energy production through nuclear reactions. The reaction products share an energy excess in the form of kinetic energy. As nuclear fusion is achieved through collisions, cross-sections play a key role. The energy of the reactants needs to be high enough to overcome the Coulomb repulsion. Because of the high cross-sections at relatively low temperatures and the high enery yield (see figure 1.1), the most promising reaction is [1]:

$$^2D +^3 T \rightarrow^4 He\ (3.5\ \text{MeV}) + n\ (14.1\ \text{MeV})$$

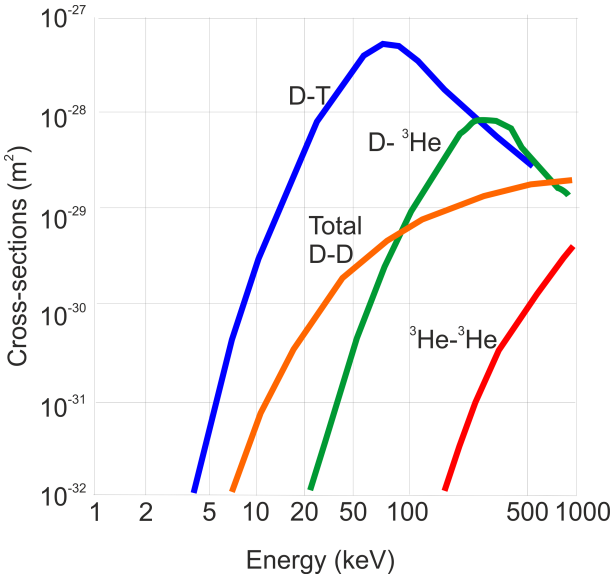

Figure 1.1: Cross-section for different fusion reactions as a function of energy. Figure taken from [2].

Given the high temperatures required, the fuel is in the plasma state. A plasma is a quasineutral gas which exhibits collective behavior. This means that particle motion (see chapter 1.4) is described through long range electromagnetic interaction rather than through collisions with neighbouring particles.

Ignition is reached when the release of fusion energy compensates for the losses, and the reaction becomes self-sustained. The Lawson criterion gives a relation between the peak ion density (n in m^{-3}), temperature[1] (T, in keV) and confinement time (τ_e, in seconds) for ignition to be achieved:

[1]Given the relation between energy and temperature by means of the Boltzmann constant, according to $T(eV) = k_B T(K)$, where the Boltzmann constant is of 11604 $K \cdot eV^{-1}$

$$n \cdot T \cdot \tau_e > 5 \cdot 10^{21} m^{-3} \cdot keV \cdot s$$

Confined fusion can be achieved, e.g. in stars, where gravitational forces balance the pressure. As it is not possible to reproduce these conditions on Earth different confinement methods need to be developed. To date, the most advanced concept is the tokamak device, based on magnetic confinement fusion in which magnetic fields are used to confine the plasma. The ITER fusion device is an international project which aims to demonstrate tokamak feasibility to produce energy. It is currently under construction in southern France.

1.3 Tokamaks

A tokamak is a toroidal plasma confinement device. To avoid particle losses (see chapter 1.4.1) a helical magnetic field is needed. It is convenient to introduce the toroidal (ϕ, around the torus) and poloidal (θ, perpendicular to it, and circling around the torus cross-section) angles, see figure 1.2, and decompose the magnetic field in its poloidal and toroidal contributions.

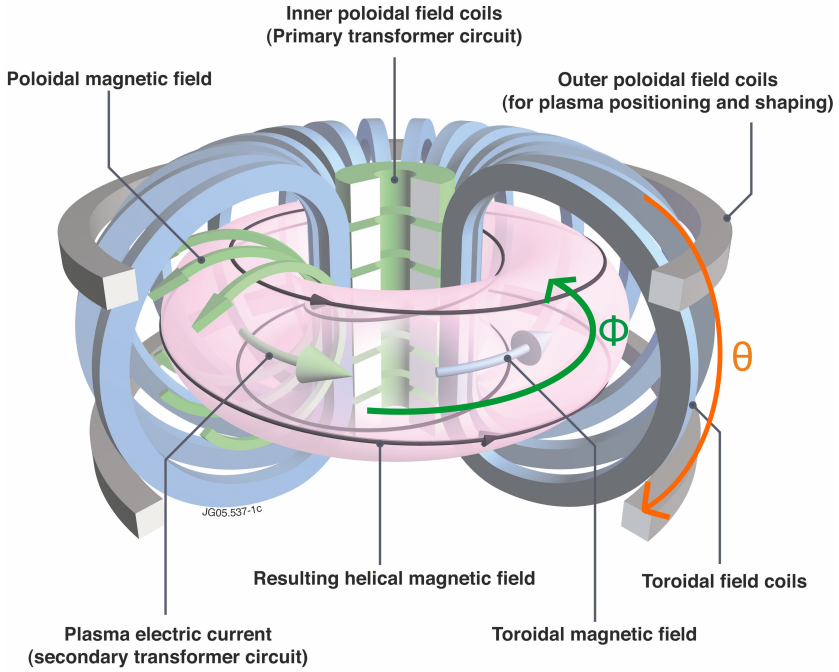

Figure 1.2: Schematics of a tokamak. Figure taken from [3].

A toroidal field (B_ϕ) is externally imposed by means of toroidal field coils (TFC). Its

dependence on the radius (from Ampere's Law, $B_\phi = \frac{\mu_0 I_T}{2\pi}\frac{1}{R}$, where R is the major radius and I_T the total current in the TFC) allows the distinction between the inner high (HFS) and outer low field side (LFS). A poloidal magnetic field (B_θ) is produced by means of a plasma driven current. The plasma acts as a secondary coil of a transformer, in which an electric field is induced by a change in the magnetic flux across the inner poloidal field coils (PFC). The experiments (also referred to as discharges) which were analysed in this thesis were carried out in the mid-size tokamak ASDEX Upgrade (located in Garching, Germany). Its main characteristics are presented in table 1.1.

Number of TFC	16
Number of PFC	12
Maximum magnetic field	3.1 T
Plasma current	0.4 MA - 1.2 MA
Major radius (R_0)	1.65 m
Minor radius (a)	0.5 m
Plasma species	D, H, He
Plasma volume	14 m^3
Plasma mass	3 mg
Electron density	10^{20} m^{-3}
Plasma temperature	up to 100 million °C (8.6 keV)

Table 1.1: ASDEX Upgrade technical data and typical plasma parameters for a discharge.

In order to achieve the high temperatures required to obtain a plasma, auxiliary heating power is needed. ASDEX Upgrade (AUG) is equipped with an installed auxiliary heating power of 30 MW, which consists of ions and electrons wave heating (up to 10 MW) and neutral beam systems (up to 20 MW). Electron (4 MW) or Ion (6 MW) Cyclotron Resonant Heating are radiofrequency waves which transfer energy to electrons (140 GHz) or ions (30 to 120 MHz) when the emission frequency matches the species cyclotron resonance frequency or its harmonics. The electron/ion population affected will afterwards transmit their energy to the plasma bulk by collisions. The Neutral Beam Injection (NBI) system is based on the injection of suprathermal neutrals which will ionize and transfer their energy to the thermal plasma via collisions. Further details of the NBI system are given in chapter 3.3, due to its relevance in the analysis of the discharges.

In an axisymmetric equilibria (that is, independent of ϕ) the internal balance between the plasma pressure and the magnetic field forces gives rise to nested magnetic flux (Ψ) surfaces, in which many quantities (e.g. the plasma potential) are constant. Figure 1.3 shows the nested structure of the flux surfaces. To label them, a variety of flux normalized coordinates can be defined. In the frame of this thesis, the normalized poloidal flux radius (ρ_{pol}) was chosen as the radial coordinate:

$$\rho_{pol} = \sqrt{\frac{\Psi - \Psi_0}{\Psi_S - \Psi_0}} \tag{1.1}$$

The subindexes S and 0 refer to the last closed flux surface (LCFS or separatrix, where $\rho_{pol} = 1$, indicated in blue in figure 1.3) and the magnetic axis ($\rho_{pol} = 0$, indicated with a red dot in figure 1.3).

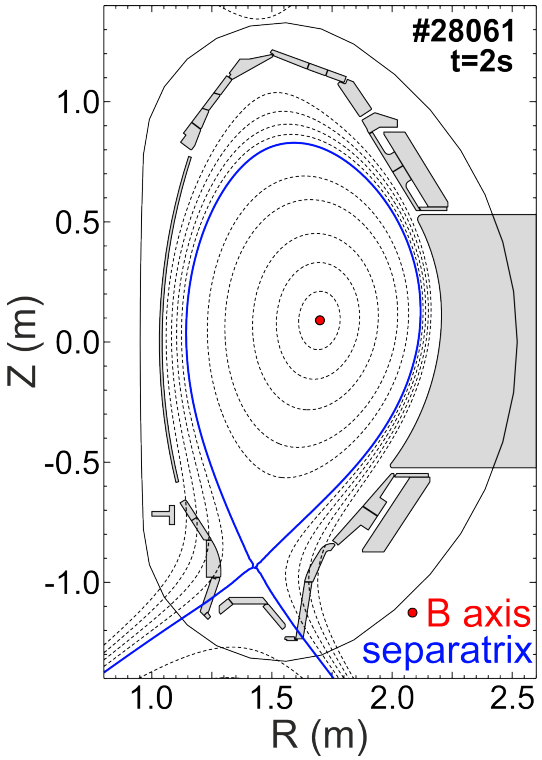

Figure 1.3: Poloidal projection of the AUG tokamak. The blue line is the last closed flux surface (LCFS), the red dot the magnetic axis. Nexted flux surfaces are indicated with dashed black lines.

1.4 Particle motion

In order to describe particle motion, we will focus on the single particle description of the plasma. The trajectories of charged particles are considered individually in the presence of magnetic and electric fields which are not modified by the presence of the charged particles. As a first approach, we assume a uniform magnetic field (no electric field) with straight field lines. The equation of motion is given by the Lorentz force and we decompose it in the directions parallel and perpendicular to the magnetic field:

$$\mathbf{F} = q \cdot (\mathbf{v} \times \mathbf{B}); \qquad m\frac{d\mathbf{v}_\perp}{dt} = q \cdot (\mathbf{v}_\perp \times \mathbf{B}); \qquad m\frac{d\mathbf{v}_\parallel}{dt} = 0 \tag{1.2}$$

The motion of a particle is constrained to a circle in the plane perpendicular to the magnetic field, moving with constant velocity parallel to it. The trajectory of the particle is a helix whose axis is usually referred to as guiding centre. The gyration of the particles around the field lines is described by means of the cyclotron frequency (ω_c) and the Larmor radius (r_L):

$$\omega_c = \frac{|q|B}{m} \qquad r_L = \frac{mv_\perp}{|q|B} = \frac{v_\perp}{\omega_c} \tag{1.3}$$

It is convenient to distinguish between the gyration of particles around the magnetic field and the trajectory of the guiding centre (see figure 1.4), which is subject to drifts.

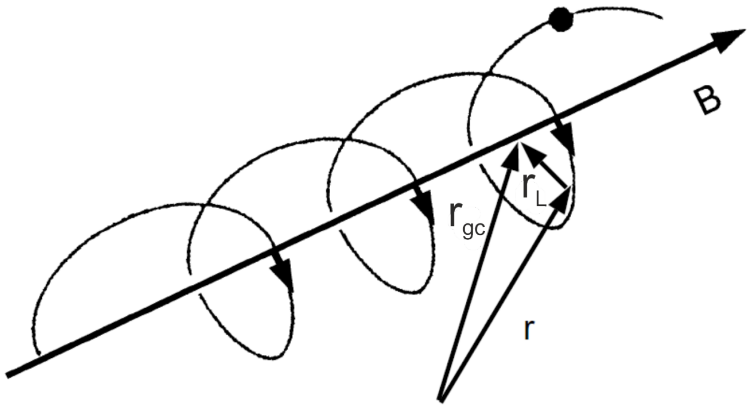

Figure 1.4: Helical orbit of a particle. Decomposition of particle motion in its gyration around the magnetic field and the motion of the guiding centre, where r is the vector position of the particle, r_L is the Larmor radius and r_{gc} the vector position of the guiding centre.

1.4.1 Drifts

When a force perpendicular to the magnetic field is present, guiding centre drifts occur. The general expression for drifts is given by:

$$\mathbf{v} = \frac{1}{q}\frac{\mathbf{F} \times \mathbf{B}}{B^2}. \tag{1.4}$$

As the magnetic field has a gradient in the direction of the major radius, an additional force perpendicular to both the magnetic field and its gradient arises and causes a drift, called ∇B-drift. It can be expressed as:

$$\mathbf{v}_{\nabla \mathbf{B}} = -\frac{m v_\perp^2}{2qB^3} \nabla B \times \mathbf{B} \tag{1.5}$$

If there is an electric field perpendicular to the magnetic field, particles will feel a force $\mathbf{F} = q \cdot \mathbf{E}$. The E×B-drift is given by:

$$\mathbf{v}_{\mathbf{E}\times\mathbf{B}} = \frac{\mathbf{E} \times \mathbf{B}}{B^2}. \tag{1.6}$$

Note that unlike the ∇B-drift, it does not depend on charge nor mass of the particle and points therefore into the same direction for ions and electrons. Because of the toroidal geometry, particles will feel a central force and a curvature drift appears. If we assume constant radius of curvature of the field lines (R_c), the average centrifugal force is:

$$\mathbf{F} = m v_\parallel^2 \frac{\mathbf{R_c}}{R_c^2} \tag{1.7}$$

The dependence of $B \propto R$ leads to $\frac{\nabla |B|}{|B|} = -\frac{\mathbf{R_c}}{R_c^2}$ [4]. Then we can express the curvature drift in terms of ∇B:

$$\mathbf{v}_{curv} = -\frac{m v_\parallel^2}{qB^3} \nabla B \times \mathbf{B} \tag{1.8}$$

Note that the curvature drift and ∇B-drift have similar expressions and are associated to parallel and perpendicular components of the velocity, respectively. They are due to the toroidal geometry and act differently on electrons and ions, leading to charge separation and the build-up of an electric field $\mathbf{E}$. Particles drift towards the tokamak wall due to the E×B-drift. To avoid particle losses, the poloidal field is introduced so that the overall effect of drifts on orbits is cancelled.

1.4.2 Particle orbits

The presence of a gradient in the magnetic field makes it possible for particles to be trapped in magnetic mirrors. In the absence of collisions, this allows the general classification of guiding centre orbits in two groups: trapped and passing. When a particle performs a periodic motion, adiabatic invariants (i.e. constants of motion) can be found. Thus, if the change in **B** is slow and on a large scale when compared to the period and the characteristic length of the particle motion, the magnetic moment becomes an adiabatic invariant. Likewise, the toroidal canonical momentum is conserved in axisymmetric magnetic field configuration.

Magnetic mirrors giving rise to particle trapping can be explained in terms of conservation of energy

$$E = \frac{1}{2}mv^2 = \frac{1}{2}m(v_\perp^2 + v_\parallel^2) \tag{1.9}$$

and magnetic moment

$$\mu = \frac{mv_\perp^2}{2B} \tag{1.10}$$

It can be illustrated as follows: when a particle moves towards regions of higher magnetic field, $v_\perp$ needs to increase so that μ remains constant. At the same time, $v_\parallel$ needs to decrease so that energy is conserved. This means that particles having low $v_\parallel/v_{tot}$ at the LFS (*trapped* particles) will reach $v_\parallel = 0$ when moving towards HFS. At this point, they will reverse movement and bounce back to the LFS because of the force $\mathbf{F}_\parallel = -\mu\nabla_\parallel B$. Particles with high enough $v_\parallel/v_{tot}$ at the LFS (*passing* particles) do not have this restriction in their movement and can fully penetrate into the HFS without reaching $v_\parallel = 0$. Poloidal projections of both trajectories are shown in figure 1.5. Because of their shape in the poloidal plane, the orbits of trapped particles are also called *banana* orbits.

The pitch angle (Λ) of a particle can be defined as:

$$\Lambda = \arccos\left(\frac{v_{||}}{v}\right) \tag{1.11}$$

which depends on the inclination of the magnetic field line. Because of the dependence of the orbit topology on the velocities ratio, particles with low pitch angle (below 30°) are considered to be passing particles and particles with high pitch angle (above 80°) are considered to be deeply trapped particles. In between, the trapped-passing boundary is found at a pitch angle that depends on the energy of the ion and its birth radial position. A

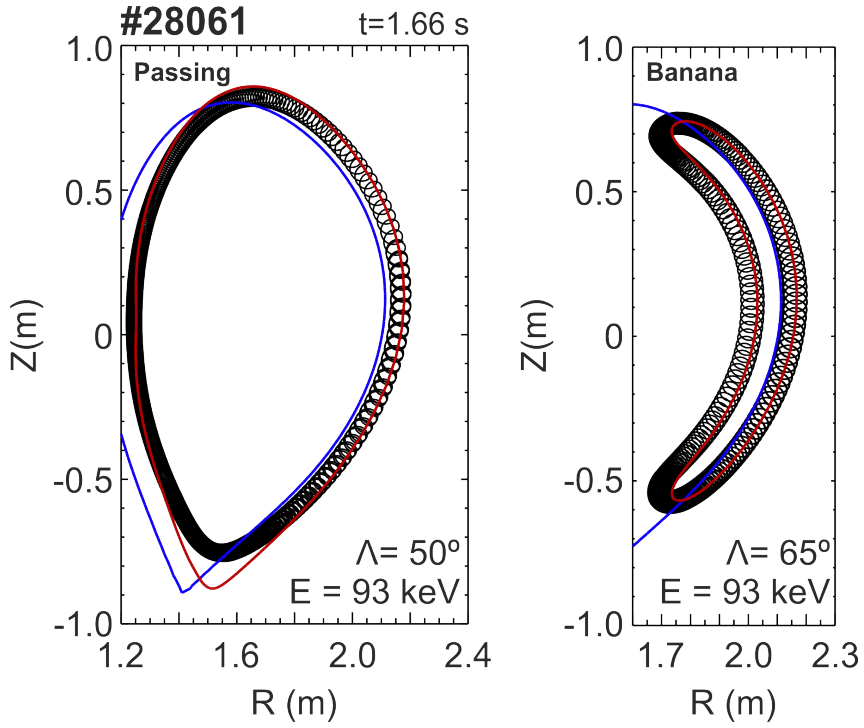

Figure 1.5: Passing and banana orbit for fast-ions of E= 93 keV. Note the impact of the change in the pitch angle (from 50 to 65º) in the orbit topology.

condition for particles to be trapped can be defined as follows [1]. We focus on a magnetic flux surface and define $v_{\perp 0}$ as the velocity of the particle where the magnetic field has its minimum (B_{min}). Because of magnetic moment conservation along the trajectory, we can write:

$$\frac{v_\perp^2}{B_b} = \frac{v_{\perp 0}^2}{B_{min}} \qquad \rightarrow \qquad \frac{B_b}{B_{min}} = \frac{v_\perp^2}{v_{\perp 0}^2} = 1 + \frac{v_{\parallel 0}^2}{v_{\perp 0}^2}$$

where B_b and $v_\perp$ are the magnetic field and the perpendicular velocity at the bouncing point, respectively. At this point $v_\parallel = 0$ and energy conservation gives $v_\perp^2 = v_{\parallel 0}^2 + v_{\perp 0}^2$. We make the approximation $B \cdot R = B_0 \cdot R_0$, where R_0 is the major radius. If we assume the magnetic field has its maximum along the flux surface at $R_0 - r$ and a minimum at $R_0 + r$ (where r is the minor radius of the magnetic flux surface), then:

$$\frac{B_{max}}{B_{min}} = \frac{R_0 + r}{R_0 - r}$$

The condition for a particle to be trapped is that $B_{max} > B_b$, which leads to

$$\frac{v_{\parallel 0}}{v_{\perp 0}} < \left(\frac{2r}{R_0 - r}\right)^{1/2}$$

The inclination of the magnetic field is usually expressed by means of the q-value of a field line. It represents the change in the toroidal angle ($\Delta\phi$) of a field line that returns to a certain position in the poloidal plane.

$$q = \frac{\Delta\phi}{2\pi}$$

The q-value represents the ratio between the number of toroidal and poloidal turns of a field line until it closes on itself. The q-value is also called safety factor because it plays an important role in stability.

The toroidal canonical momentum (P_ϕ) is conserved in axisymmetric magnetic field configuration. It is given by:

$$P_\phi = mRv_\phi - Ze\Psi$$

where v_ϕ is the toroidal velocity, R the major radius, e the electron charge, Z the atomic number and Ψ the poloidal flux. Its conservation follows from toroidal symmetry and its constancy implies a small displacement of particles across the flux surface in their orbits. Its variation due to magnetic perturbations is shortly presented in chapter 2.3.

1.5 Objectives

This thesis aims to help in the understanding of plasma response to externally applied 3D fields, also referred to as magnetic perturbations (MPs). This thesis is focused on the impurity toroidal rotation, fast-ion losses and density response to MPs. The interdependencies between these parameters have been analysed. Plasma response to MPs is a very active research line, as MPs are used for instability control and enable mitigation/suppression of edge localized modes (ELMs).

MPs break the symmetry of the magnetic field and can enhance edge radial transport and induce density pump-out (i.e. a drop in the density profile) [5]. Particle losses can create a current and therefore lead to plasma flows. The plasma responds with non-ambipolar fluxes in order to maintain quasi-neutrality. This gives rise to a change in the radial electric field (E_r). The interaction of E_r with the perturbed magnetic field can affect the edge plasma rotation (by means of the E×B drift). Likewise, the corrugation of magnetic field lines produced by MPs can modify particle orbits, affecting their confinement. In this way, changes in the fast-ion losses are also expected [6], [7].

The scope of this thesis is a correlation study regarding toroidal velocity, fast-ion losses and density. For this purpose, two discharges performed at the ASDEX Upgrade tokamak, with different toroidal magnetic field, equal auxiliary heating input and similar magnetic perturbation configurations are analysed. The coupled time evolution of toroidal impurity rotation, fast-ion losses and plasma density is studied during the application of MPs. The effect of varying the neutral beam injection sources, which generate the fast-ions in these discharges, has been addressed.

Chapter 2

Theoretical background

2.1 H-mode

Above a certain power threshold, the plasma transits from a low confinement regime (L-mode) to a high confinement regime (H-mode), which has improved energy confinement times [8]. The H-mode was first discovered on ASDEX in 1982 [8] and is nowadays the baseline operational scenario in most tokamaks. During the transition from L to H-mode, a sudden increase in plasma energy and density together with a drop in D_α emission (i.e. a drop in particle transport) is observed [9]. The H-mode is characterized by the development of a region of suppressed turbulence in the plasma edge (the Edge Transport Barrier, ETB, which is highlighted in blue in figure 2.1).

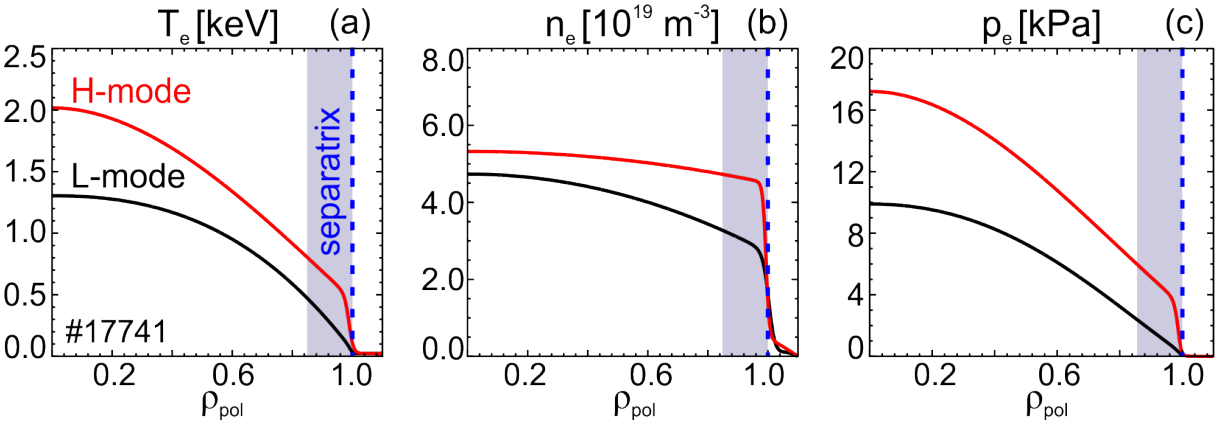

Figure 2.1: Comparison of L and H-mode profiles. The ETB is highlighted in blue. The plasma centre is at $\rho_{pol} = 0$ and the plasma edge towards $\rho_{pol} = 1$. Figure taken from [10].

The establishment of a transport barrier triggers instantaneous changes in the plasma

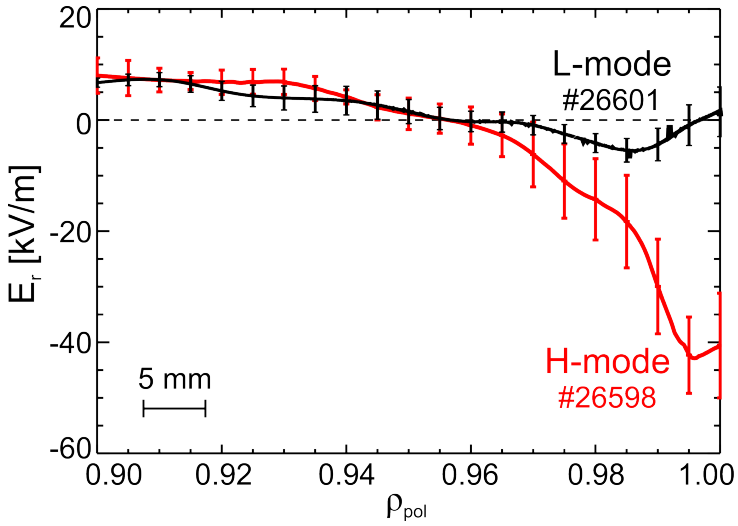

Figure 2.2: Comparison of E_r in L and H-mode. Figure taken from [10].

edge. A pedestal structure in temperature, density and pressure (as a consequence of temperature and density) profiles is developed just inside the separatrix. Besides, a deep well in the radial electric field (E_r) emerges (see figure 2.2). It is widely accepted that the steep gradients in E_r suppress turbulence at the edge and lead to the formation of the ETB. This is due to a shear in the particle flow within the edge region, which can break up the turbulent eddies. The typical width of the well is 1.2 ± 0.2 cm at AUG [10]. In H-mode regimes, the radial electric field is negative at the edge. This means that it points towards the inside of the plasma and thermal ions are electrostatically confined.
The ambipolarity condition demands the radial drift of electrons and ions to be balanced ($u_{r,i} = u_{r,e}$) [11]. In the presence of external forces that lead to non-ambipolar fluxes, E_r is set such that the ambipolarity condition is fulfilled, i.e. E_r is not a free parameter. Thus, a change in the E_r can be driven by e.g. NBI or magnetic perturbations, as they induce an external force which can act differently on ions and electrons. Experimentally, E_r can be reconstructed by means of charge exchange recombination spectroscopy (CXRS) measurements, which provide temperature, density and velocity measurements, [12] (see chapter 3.1.1), and the radial force balance equation:

$$E_r = \frac{1}{n_\alpha q_\alpha}\frac{\partial p_\alpha}{\partial r} - v_{\theta,\alpha}B_\phi + v_{\phi,\alpha}B_\theta \tag{2.1}$$

Here, α is the considered species, n is the density, q the charge, $\partial p/\partial r$ the radial pressure gradient, B the magnetic field and v the velocities. Subindexes θ and ϕ refer to poloidal and toroidal direction, respectively. For the considered discharges, the calculation of E_r was not possible because detailed measurements of the edge impurity v_θ were not available.

In the edge, the impurity v_θ is the dominant term in the radial force balance equation and can not be neglected. Thus, the study is focused on the effect of MPs on toroidal rotation (v_ϕ), which is related to E_r.

2.1.1 Edge Localized Modes

The onset of the H-mode is accompanied by edge localized modes (ELMs). ELMs are periodic magnetohydrodynamic (MHD) instabilities which lead to a reduction of stored energy and a degradation of the plasma confinement. During an ELM, particles and energy are lost to the wall. ELMs can be beneficial to control impurity/particle transport. ELMs are believed to be triggered when the peeling-ballooning stability boundary is exceeded [13], [14]. The peeling-ballooning stability boundary is based on a limit in the edge current and edge pressure gradient, respectively. Because of the heat flux to the wall, ELM mitigation and suppression techniques are needed in order to avoid damage to the plasma facing components. The application of external 3D magnetic perturbations is to date the ELM mitigation technique considered for ITER, as explained in chapter 2.3.

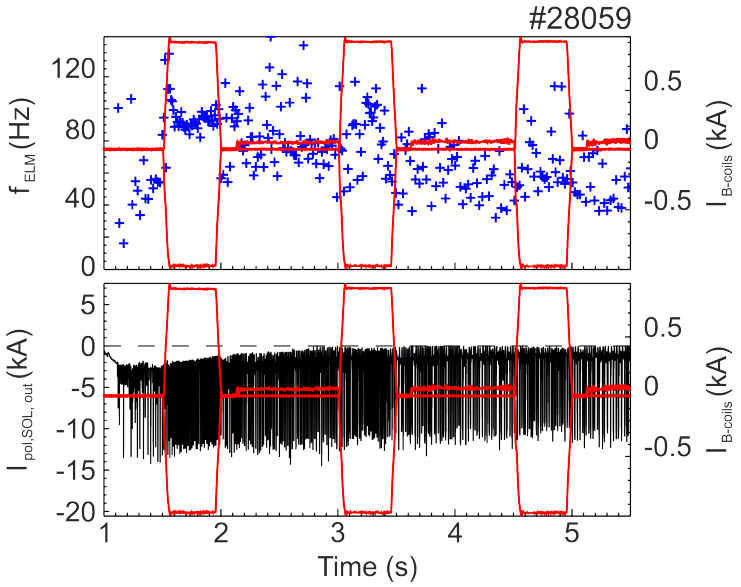

Figure 2.3: (a) Outer divertor thermocurrent amplitude and (b) ELM frequency (f_{ELM}) time-trace for discharge #28059. The currents circulating through the B-coils, which produce the magnetic perturbation, are shown in red.

ELM mitigation can be achieved by means of increasing their frequency. More frequent and smaller ELMs would lead to lower losses associated to each ELM. ELMs can be measured by means of the thermocurrents in the outer divertor ($I_{pol,SOL,out}$), as they are an indicator of divertor heat loads due to ELMs. In the figures 2.3 and 2.4, the temporal

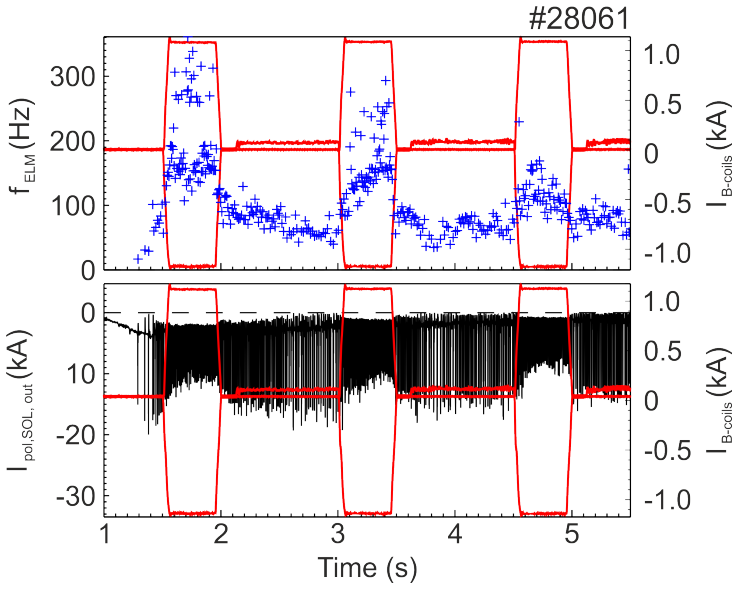

Figure 2.4: (a) Outer divertor thermocurrent amplitude and (b) ELM frequency (f_{ELM}) time-trace for discharge #28061. ELM mitigation seen as a modulation of the amplitude (decreases) and frequency (increases) during the MP phases. The currents circulating through the B-coils, which produce the magnetic perturbation, are shown in red.

evolution of $I_{pol,SOL,out}$ in amplitude and the ELM frequency for the two discharges analysed during this thesis are shown. The blue and red lines show the currents circulating in the B-coils, which induce the magnetic perturbation (see chapter 2.3). We can see how the application of magnetic perturbations has the consequence of reducing the amplitude of the thermo-current and increasing ELMs frequency. The effect is most evident for discharge #28061, for which ELM mitigation phases are achieved.

2.2 Fast-ions

Fast ions are supra-thermal ions, i.e. ions with energy higher than the plasma bulk. They can be generated mainly in three ways: fusion products, NBI injection and radiofrequency heating. As future plasmas are expected to be heated by means of α-particle fusion products, its confinement during sufficiently long times is essential, so that their energy can be transferred to the plasma bulk. A good confinement of fast-ions is also important to guarantee the integrity of plasma facing components, as the fast-ions would deposit their high energy onto the vessel when escaping. For these reasons, understanding the mechanisms of generation and confinement/loss of fast-ions is crucial.

For the analysed discharges, fast-ions are generated by means of NBI. Suprathermal neu-

trals are injected to the plasma bulk and will undergo ionization via charge exchange reactions and electron impact ionization. As the energy involved in ionization processes is low, the ion birth energies will be similar to the neutral injection energies. The NBI is not only important because it determines the ion birth energy, but also the ion's pitch angle. As the pitch angle is determined by $v_{\parallel}$ and the local magnetic field, the NBI injection geometry plays an important role and can determine whether an ion will be born in passing or trapped orbits.

Fast-ion losses can be measured by means of a fast-ion loss detector (FILD, see chapter 3.1.2). NBI fast-ions can be born in open orbits and directly lost to the wall. These are the *prompt losses*. In the absence of any perturbations, FILD measures escaping ions due to prompt losses. The following figures (2.5, 2.6) show ASCOT simulation results of the birth location of fast-ions generated by NBI Q7 which are detected afterwards in FILD. Note that this discharge is similar to the ones analysed in this thesis and illustrates where fast-ions detected in FILD are born.

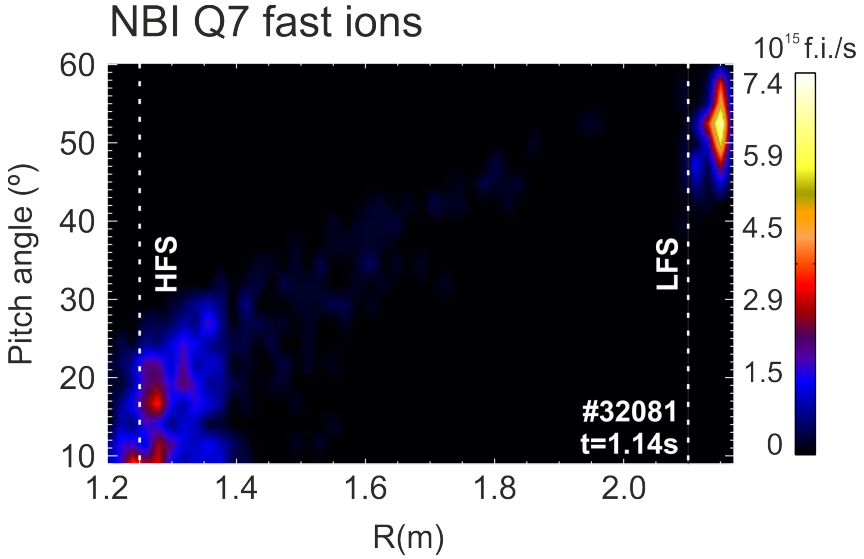

Figure 2.5: ASCOT simulations for discharge #32081 at time 1.14s (without MP) showing NBI Q7 born fast-ions that strike on FILD, as a function of the birth radial position and their pitch angle.

According to figure 2.5, ions in the HFS show low pitch angle (below 30°, so mostly passing) and ions in the LFS show higher pitch angle (between 40° and 60°, and thus around the trapped-passing boundary). We see in figure 2.6 (a) that the toroidal location is also different for ions born in the LFS (close to FILD) and HFS (centered around $\phi = 260°$). By looking at figure 2.6 (b) it becomes clear that ions are born in the plasma edge ($\rho_{pol} > 0.9$) for both LFS and HFS. The detection of ions with FILD can be

simplified as follows: ions born in the LFS will follow trapped orbits having short toroidal displacement before they collide with FILD while ions in the HFS will follow their passing orbits moving towards FILD poloidally and toroidally until they finally reach it.

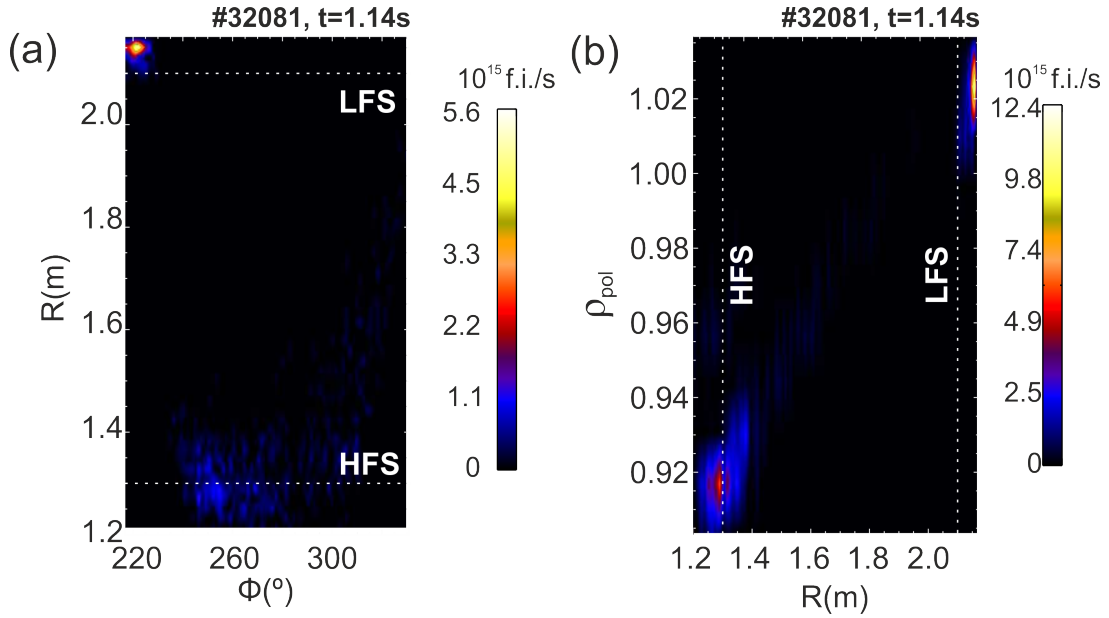

Figure 2.6: ASCOT simulations for discharge #32081 at time 1.14s (without MP) showing the birth location of NBI Q7 born fast-ions that strike on FILD, as a function of (a) the birth radial position and the toroidal angle (ϕ) around AUG and (b) the birth radial position and normalized flux radial coordinate ρ_{pol}.

It is important to point out that the ionization rate depends on the density of the plasma, the beam density and the process cross-section (which depends on the relative velocity between the particles) [1]. Because of the strong gradient of plasma density at the edge, the NBI deposition is peaked there. Figures 2.5 and 2.6 show the NBI generated ions that are detected in FILD. The deposition profile of an NBI is shown in figure 2.7. The application of the magnetic perturbations leads to a reduction of the plasma density. It can be noted that the lower the density, the deeper the NBI deposition. Note that fast-ions shown in figures 2.5 and 2.6, fulfil the condition of being born by NBI Q7 and being detected in FILD, while fast-ions shown in figure 2.7 do not fulfil the second condition. Thus, figure 2.7 shows all fast-ions deposited by the NBI.

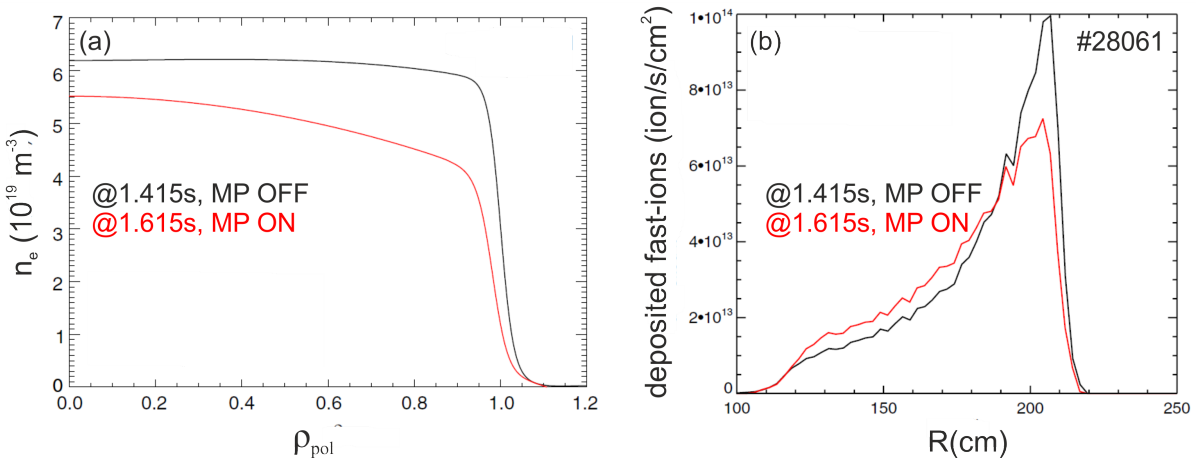

Figure 2.7: (a) Density profiles before and during the application of magnetic perturbations. As can be seen, magnetic perturbations lead to a reduction of plasma density (density pump-out). (b) Radial birth density of NBI fast-ions. We can see that lower density implies deeper NBI deposition. Figure taken from [6].

2.3 Magnetic perturbations

Magnetic perturbations (MPs) can be applied in order to counteract the effect of error fields, which would cause a deviation from the axisymmetric configuration of the magnetic field [15]. Error fields can emerge from various reasons, e.g. toroidal field ripple due to discontinuities in the toroidal magnetic field or tolerances in the installation of field coils. Moreover, the application of non-axisymmetric 3D fields has been proved to be one of the most effective tools to mitigate and even suppress ELMs without degrading H-mode confinement [16], [17], [18]. MPs create stochastic regions in the edge (in a simple picture, will create magnetic islands) and enhance particle transport through the pedestal [5]. In this way, pressure gradients are reduced and reaching the ELM stability limit is avoided. MPs show a different effect on kinetic profiles depending on collisionality. The collisionality is a dimensionless parameter that reflects the role of collisions in transport. It is expressed as the effective collision frequency normalized to the trapped particle bounce frequency:

$$\nu^* = \frac{\nu_{eff}}{\omega_b} \tag{2.2}$$

In low collisionality regimes, particles can complete several banana orbits without colliding, while in high collisionality regimes they will collide before completing an orbit. The collisionality is proportional to the density and inversely proportional to the temperature squared ($\nu_j^* \propto \frac{n_j}{T_j^2}$, where j holds for the species).

MPs have shown a strong impact on density profiles, rotation and fast-ions in H-mode low collisionality discharges [6], while they show no significant effect in the parameters in high collisionality discharges. The effect of MPs on different parameters is shortly presented:

- **Electron density**: Enhanced (suppressed) particle transport produces density pump-out (in) phenomenon, which is observed as a general drop (rise) in electron density at the plasma edge and core.

- **Toroidal rotation and radial electric field**. Because of stochastic regions, electrons leave the plasma and cause a radial ion current to balance electron losses. No significant effect on E_r due to the MPs has been observed in high collisionality H-mode discharges [19]. In L-mode low collisionality discharges, resonant MPs show a different response outside and inside the separatrix, where E_r reverses (becomes positive) and its peak is reduced, respectively [20].

- **Toroidal canonical momentum**: The MP poloidal spectra has an effect on the toroidal canonical momentum of the fast-ion, affecting the fast-ions transport (radially inwards/outwards transport) [21]. Positive (negative) variations of toroidal canonical momentum produce inward (outward) transport, which is expected to improve (degrade) the confinement of fast-ions.

- **Fast-ion losses**: In the presence of an axisymetric magnetic field, fast-ions are in general well-confined. Deviations from an axisymmetric configuration have an impact on the fast-ion losses [6], [7]. The MP will kick ions in their orbits, and thus ions that were initially confined in the absence of perturbations can be lost when MPs are applied.

Chapter 3

The experiment ASDEX Upgrade

In the following chapter, a description of the diagnostics and systems which are relevant to the analysis is presented. In figure 3.1, a toroidal (left) and poloidal (right) view of the tokamak showing the location of the described diagnostics and systems is included.

3.1 Diagnostics

To reveal the correlations between toroidal rotation, plasma density and fast-ion losses, the measurements from different diagnostics need to be combined. The following diagnostics provided the required measurements.

3.1.1 Charge Exchange Recombination Spectroscopy

Charge Exchange Recombination Spectroscopy (CXRS) is the most common technique to measure ion temperature and rotation in tokamaks [22]. The basic principle relies on the charge transfer between fully-ionized impurities and neutrals, which leaves the impurity ion in an excited state. It subsequently decays to the ground state, thereby, emitting a photon. The analysis of the emitted spectrum yields information about different parameters such as temperature, density and velocity of the observed species. The charge exchange reaction can be described as:

$$A^{Z+} + D \quad \rightarrow \quad A^{(Z-1)+*} + D^{+} \quad \rightarrow \quad A^{(Z-1)+} + D^{+} + h\nu$$

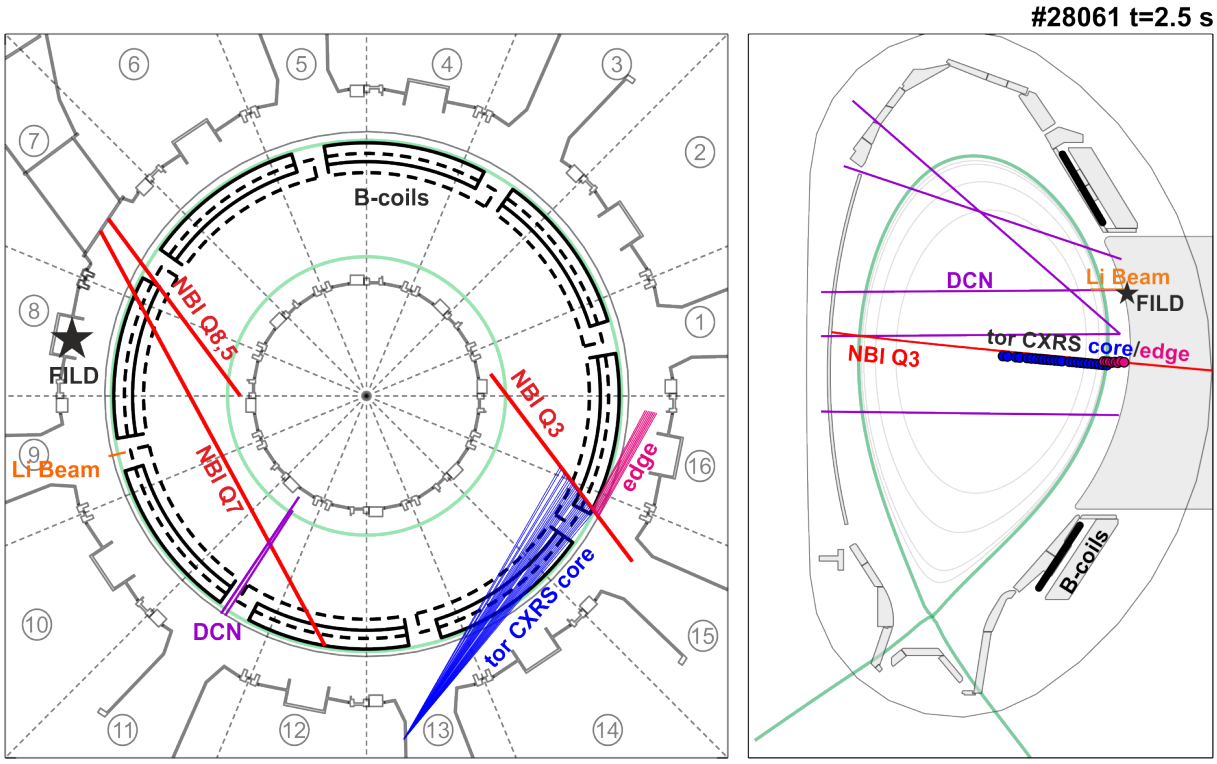

Figure 3.1: Arrangement of the diagnostics and neutral beam injectors (red) that were used in the analysed discharges and B-coils (black) at AUG. The separatrix is shown in green.

The CX reaction typically takes place between neutral atoms from neutral beam injection (D, H) and completely ionized impurities. Low-Z impurities (such as B^{5+} or C^{6+}) are preferred because they are fully-ionized at all radial positions and in higher concentrations than high-Z impurities. The photons are emitted at characteristic energies for each species (α), giving rise to a measured spectrum which can be fitted to a Gaussian distribution (see figure 3.2). From the fitted spectra, the temperature, density and rotation of the impurities are determined.

The intersection between the neutral beam and the lines of sight of the diagnostic determines the location of the collected signals. The difference between the theoretical wavelength (λ_0) and the measured wavelength due to the Doppler effect ($\Delta\lambda$) allows us to determine the velocity of the given impurity species:

$$\frac{\Delta\lambda}{\lambda_0} = \frac{v_{rot,\alpha} \cdot \mathbf{e}_{LOS}}{c} \tag{3.1}$$

where $\mathbf{e}_{LOS}$ is the unit vector along the LOS and c the speed of light. The ion temperature (T_α) is related to the width of the distribution according to:

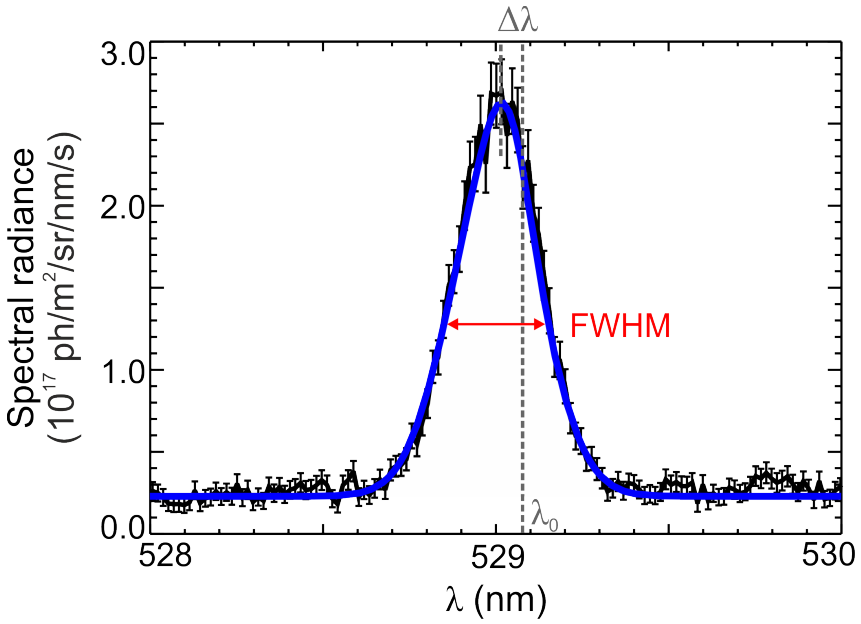

Figure 3.2: Example of a carbon spectrum obtained with CXRS and its Gaussian fit. The temperature and velocity of the species can be obtained by means of the FWHM and the Doppler shift, respectively. Figure taken from [10].

$$T_\alpha = \frac{m_\alpha c^2}{8ln(2)\lambda_0^2 e^2} FWHM^2 \tag{3.2}$$

where FWHM is the full width at half maximum, m_α the mass of the species, c the speed of light and e the electron charge.

For this thesis, measurements from the edge and core toroidal CXRS systems installed at AUG have been used [12]. The LOS of these systems intersect the path of NBI Q3, which is used as diagnostic beam. The edge (core) system has a radial resolution of 1-3 mm ($\sim$ 1.5 cm) and a temporal resolution of 2.3 ms (3.5 ms). For the edge system the time resolution can be turned down to 50 μs [23].

3.1.2 Fast-Ion Loss Detector

Fast-ion loss detectors (FILD) based on scintillator materials are used in various fusion devices [24]. FILD uses the magnetic field to scatter charged particles, so that they impact on different positions on the scintillator plate depending on their pitch angle and energy. Figure 3.3(a) shows differences in the striking point depending on fast-ion pitch angle and energy. The light emitted by the scintillator material (due to its interaction with the charged particles striking into it) is directed by means of a set of lenses to the

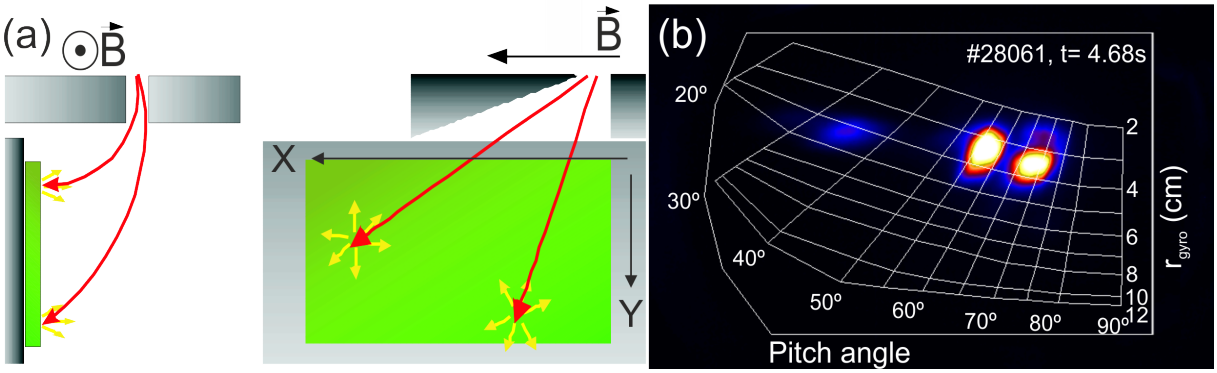

Figure 3.3: (a) Diagram showing differences in the striking positions of fast-ions onto the scintillator plate. Particles with large gyroradius impact the scintillator plate further away from the pinhole in the Y direction. Particles with higher parallel velocity (lower pitch angle) will strike further from the pinhole in the X direction. Figure taken from [26]. (b) Frame of the CCD camera for a given time point with its corresponding overlayed strike-map.

data acquisition systems. A beam splitter is used to divide the light beam in two paths. For the analysed discharges, the experimental set up was as follows: one light beam was directed to an array of 20 photomultiplier tubes and another to a CCD camera [25].

The main components of the detector head are the collimator and the scintillator material. The collimator limits the range of pitch angle and energy of the fast-ions to be detected. The choice of the scintillator material needs to be made such that high temporal resolution is possible, i.e. short decay times are needed.

High resolution in the velocity space of the particles is possible by means of the CCD camera, which has a temporal resolution of 20 ms. In order to identify the energy and pitch angle corresponding to the different hotspots, strike maps have to be generated and overlayed to the CCD image. These strike-maps are generated using IDL routines [27]. Figure 3.3(b) shows an image of the CCD camera with its corresponding overlayed strike-map. Note that the gyroradius is not the same as the Larmor radius, i.e., the radius of gyration around the magnetic field line, but its expression is $r_{gyro} = \frac{\sqrt{2mE_T}}{qB}$, which is an indicator of the total energy of the particle (E_T). The resolution in pitch angle remains constant while the resolution in energy decreases when increasing the gyroradius (the collimator efficiency decays for broad orbits). The photomultiplier tubes array allows higher temporal resolution (1 μs), but has lower resolution in velocity space. For this thesis, measurements from FILD1, located in sector 8, have been used.

3.1.3 Integrated Data Analysis

The electron density (n_e) profiles are provided by the Integrated Data Analysis (IDA) technique [28]. IDA combines measurements from different diagnostics, taking advantage of their characteristics (complementary diagnostics which measure at the plasma edge and core), and computes electron profiles reducing the uncertainties. IDA reconstructs the whole density profile taking edge measurements from a lithium beam diagnostic and line integrated core measurements from interferometry. IDA allows spatially and temporally resolved profiles with high resolution and improves data reliability.

Lithium beam diagnostic The injection of a lithium beam at high energies enables the measurements of electron density profiles at the plasma edge [29]. The lithium atoms collide with the plasma particles and are excited through these collisions. This results in light emission due to its subsequent decay. The intensity of the emission line is related to the electron density. This technique is limited to the plasma edge (around $\rho_{pol} > 0.95$) due to the attenuation of the lithium beam as it penetrates into the plasma. The spectroscopy on a lithium beam allows high spatial (5 mm) and temporal (50 μs) resolution.

DCN interferometry Another diagnostic for measuring the electron density is the interferometry technique [30]. The phase shift between a wave propagating in vacuum and one that propagates through the plasma is related to the plasma density, i.e. the interference pattern between both electromagnetic waves can be used to determine the line integrated electron density. At AUG, 5 deuterium cyanide (DCN) lasers are used for the reconstruction of core electron density with a temporal resolution of 300 μs.

3.2 B-Coils

Magnetic perturbations are induced in AUG by a set of in-vessel saddle coils, also called B-coils. The B-coils sum up a total of 16 coils which are placed in two arrays (upper and lower row) around the vacuum vessel in the LFS [31]. The B-coils are capable of generating magnetic perturbations (MPs) with toroidal mode numbers $n = 0, 1, 2, 4$ (n refers to the number of cycles which are completed within a toroidal turn). By means of varying the configuration of the coils, parity and differential phase (phase difference between the upper and lower circulating currents) a variety of perturbations can be induced.
Depending on the alignment of the MP with the pitch of the local magnetic field, resonance conditions can be achieved, as the angle between the MP and the local field line determines

the absolute value of the magnetic perturbation. Higher resonances are achieved by means of good alignment of the perturbation with the local field on rational surfaces. The maximum normalized perturbation field b_r/B is $\sim 10^{-3}$ for a typical -2.5 T operation. Figure 3.4(a) shows a scheme of the B-coils installed in AUG. In the analysed discharges, the differential phase (shown in figure 3.4(b)) between the two arrays was fixed during the MP phases to $\Delta\phi = 180°$, giving rise to a static perturbation. The configuration of the coils was odd-parity $n = 2$. The same configuration was used for both analysed discharges.

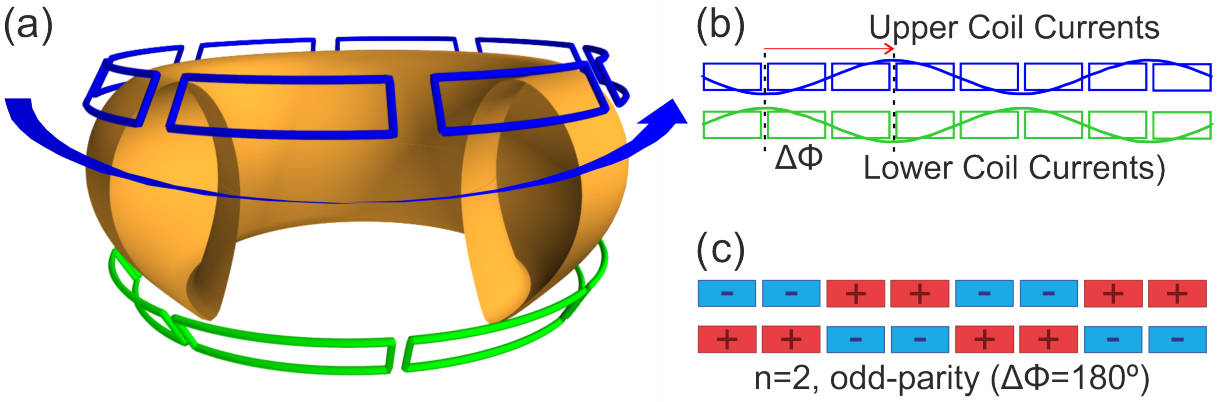

Figure 3.4: (a) B-coils at ASDEX Upgrade. Figure taken from [32]. (b) B-coils currents and the differential phase ($\Delta\phi$). (c) Parity of coils giving rise to the MP structure for the analyzed discharges in this thesis.

3.3 Neutral Beam Injection

At AUG, two neutral beam injection (NBI) boxes (also referred to as injectors) are installed, which count with a total power of 20 MW (each box has 4 sources with 2.5 MW each). The three beam energy components arise due to the generation of molecular deuterium (D^+, D_2^+, D_3^+) in the ion positive source, resulting in populations of the complete (E_0), a half ($E_0/2$) and a third ($E_0/3$) of injection energy. The injectors have a similar set-up but are located at different toroidal locations around the tokamak. In addition, there are important differences regarding the geometry of the sources, which leads to the classification of the sources in radial (2), tangential (4) and current drive (CD) (2) beams, ordered from the most normal to the most tangential injection direction. The use of more tangential injection directions favours the $v_{||}$ of the injected ions, and thus the generation of fast-ions in trapped orbits is reduced. The main characteristics of the injectors and their lines are summed up in table 3.1. In the analysed discharges, four different NBI

sources were used. NBI Q3 was always switched on for diagnostic purposes (see chapter 3.1.1). NBI Q8, Q7 and Q5 went on in successive periods. The beam lines of the four beams used for the analysed discharges are shown in figure 3.1.

	Injector 1		**Injector 2**	
Sector	15		7	
Number of sources	4		4	
Extraction voltage	60 kV		93 kV	
Ratio ($E_0 : E_0/2 : E_0/3$) (%)	65:25:10		62:29:12	
Power per source	2.5 MW		2.5 MW	
Sources and geometry	1	Radial	5	Tangential
	2	Tangential	6	CD/Off-axis
	3	Tangential	7	CD/Off-axis
	4	Radial	8	Tangential

Table 3.1: Technical data of NBI injectors at AUG. The information is taken from [33]. Beams 6 and 7 are off-axis beams, the other beams are on-axis, i.e. their beam line crosses or is close to the magnetic axis.

Chapter 4

Description of the discharges

Two low collisionality H-mode discharges (#28059, #28061) are analysed in this thesis. In this section, a description of these discharges is given. Both discharges have a similar set-up. Three 1500 ms-phases follow each other, during which the NBI source is changed. The total NBI power and fuelling are kept constant within the different phases. In the middle of each phase, MPs are applied for 500 ms. In this way, the effect of MPs when different NBI beams are used can be studied. The switch-on and switch-off of the B-Coils and the time evolution of toroidal impurity rotation, fast-ion losses and plasma density are shown in figure 4.1. The different NBI phases are indicated with colours (red, blue and gray) and during each of them a darker shaded phase indicates when MPs are applied.

The main differences between both discharges are the toroidal magnetic field and the current of the B-coils (which determine the amplitude of the MP). The toroidal magnetic field, which is the dominant contribution to the magnetic field, is of -2.45 T for discharge #28059 and -1.73 T for discharge #28061. The negative sign indicates the toroidal magnetic field is pointing clockwise in a top-down toroidal view of AUG (standard configuration). Although the configuration of the B-coils during MP phases was the same (n=2 odd-parity), the circulating current in the B-coils is different for the discharges, being 1 kA for discharge #28059 and 1.2 kA for discharge #28061. Due to a higher $I_{B-coils}/B_{\phi}$ ratio (i.e. a higher relative perturbation) the effect of MPs on density, rotation and fast-ion losses profiles in discharge #28061 is stronger compared to discharge #28059.

The evolution of the toroidal impurity rotation and density at different radial positions

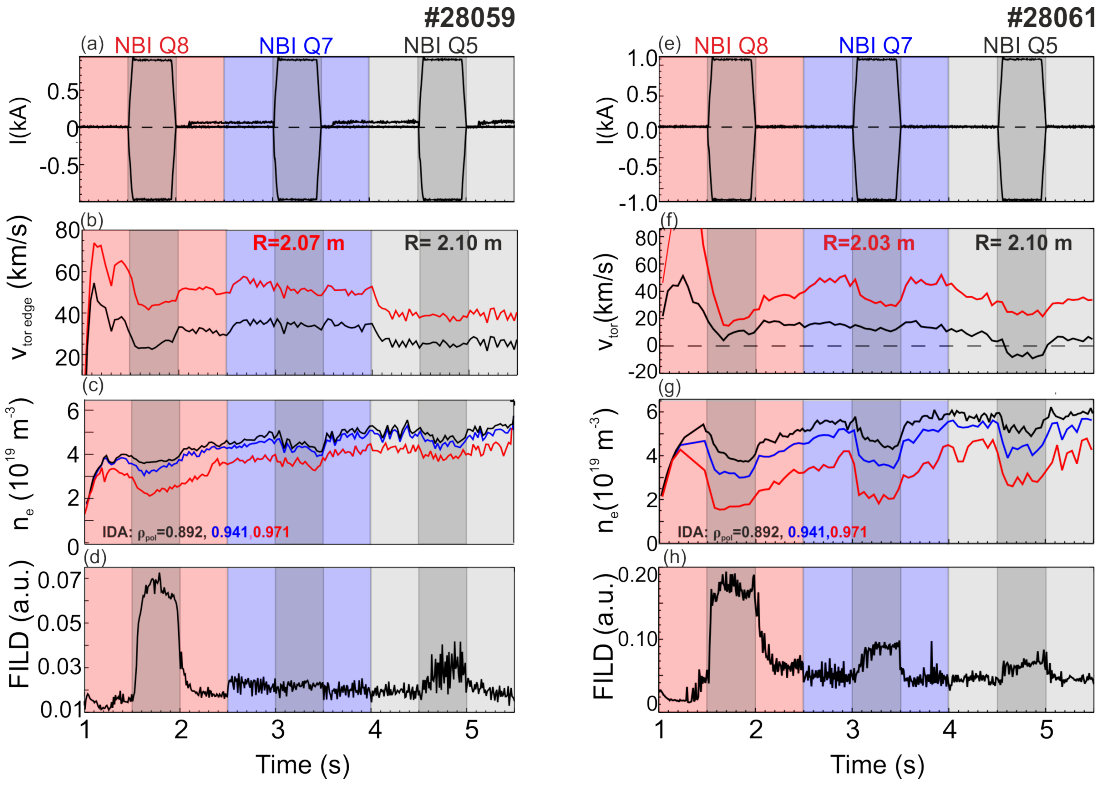

Figure 4.1: Temporal evolution of B-coils current (a),(e), toroidal impurity rotation (b),(f), density (c),(g) and fast-ion losses integrated in the velocity space (i.e. the signal of all photomultiplier tubes is summed up) (d),(h) for discharges #28059 (left) and #28061 (right).

are shown in figures 4.1(b) and (f) and 4.1(c) and (g), respectively. Figures 4.1(d) and (h) show the fast-ion loss integrated in velocity space from FILD (here, the signal from all photomultiplier tubes is summed up). During both discharges, the phenomenon of density pump-out (figures 4.1(c),(g)) and toroidal rotation braking (figures 4.1(b),(f)) during the MP phases are observed. Moreover, during the last MP phase of discharge #28061 an impurity acceleration in the counter-current direction is observed at the edge (black signal, figure 4.1(f)). This is not seen in discharge #28059, where the toroidal rotation values are always above zero. The response of the fast-ion losses is also clearly correlated to the application of MPs, as can be seen in figures 4.1(d),(h).

4.1 Temporal response to MPs

The first step towards the analysis of the coupled evolution of the parameters of interest (toroidal rotation, density and fast-ion losses) to MPs is to observe how rapidly they respond to the externally applied perturbation and whether they respond on the same time

scale. A qualitative analysis of response times was done for this purpose. The parameters are expected to respond within transport time scales, which are of the order of 60-80 ms. Figures 4.2, 4.3 and 4.5 show the temporal evolution of density, toroidal rotation and fast-ion losses for discharge #28061, respectively. Similar time scales are seen in discharge #28059 but are not presented for simplicity and because of more pronounced effects in #28061.

The ramp up and down of the B-coils current takes 50 ms. For the analysis of the response times, decay/rise times start to count from when the B-coils current has reached a stationary level and are highlighted in the figures with gray shades. The response times depend on plasma response to the magnetic perturbations and the effect of the passive stabilization loop (PSL, a conductor around the vacuum vessel in which mirror currents are induced after fast transients in the B-coils currents). In order to decouple the effects of plasma response to the B-Coils and the PSL, the B-coils need to be switched off in a configuration that compensates for the induced currents [34].

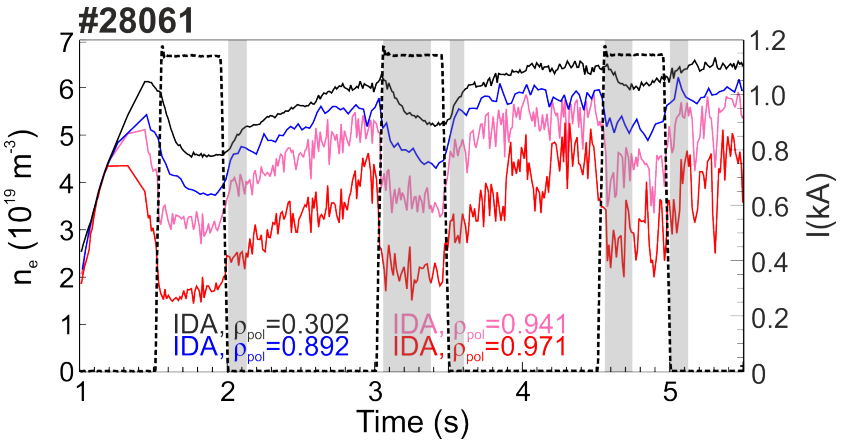

Figure 4.2: Temporal evolution of electron density at different radial positions. Measurements from core and edge IDA are shown. The rise and decay times are highlighted with gray shaded regions. The B-coils current is shown in a dashed line in the background for reference.

During both discharges, the density is overall rising and the absolute density pump-out becomes smaller. This could mean that the perturbation is shielded because of higher densities. The electron temperature (not shown in the figures) is slowly decreasing during the discharge and mostly unaffected by the perturbations. This yields an inverse dependence of density pump-out with density/collisionality. The ion collisionality (the collisionality values presented in this thesis are given at $\rho_{pol} = 0.95$) for discharge #28059 rises from 0.206 to 0.976. For discharge #28061, it increases from the first to second phase, and

decreases for the last phase. Figure 4.2 shows that the density response times are different in the edge and core of the plasma. Close to the separatrix, the density response is mostly simultaneous to switching on the B-coils (at $\rho_{pol} > 0.94$) and rapidly increases inwards (note that the decay times at the edge $\rho_{pol} = 0.89$ are of the same order of magnitude than in the core), being around 200 ms long for the core. In [34], a time constant of ~ 250 ms is found for a similar discharge ($I_p = 0.8$ MA, $B_\phi = -1.85$ T, $n_e = 5.68 \cdot 10^{19}$ m^{-3}) at $\rho_{pol} = 0.88$, in agreement with the observations for this discharge. The recovery times are of the same order of magnitude for edge and core (≈ 100 ms). Thus, depending on the radial position, the decay times can be lower/higher than the rise times. Besides, the density reaches a mostly constant stage in the middle of the MP-phase.

Regarding the response times in rotation, a more homogeneous pattern is observed. The MPs show a clear effect on rotation in discharge #28061 and little effect in discharge #28059. We observe decay times of ~ 200 ms while the rise times are ~ 100 ms. The saturation phase within the MP phase is more clearly reached for the rotation. It is interesting to notice that although the rotation evolves similarly in all radial positions and a rotation braking is observed, in the last phase, an acceleration is seen at the edge. This is clearly observed during the last phase for the LOS looking at R=2.10 m in figure 4.3. Further comments regarding rotation acceleration are made in section 4.2. Note that the first MP phase is affected by a core MHD mode during discharge #28061, which strongly affects rotation as can be seen in the figure (rotation starts to decrease before the B-coils are switched on). For this reason, this phase is not considered for the analysis.

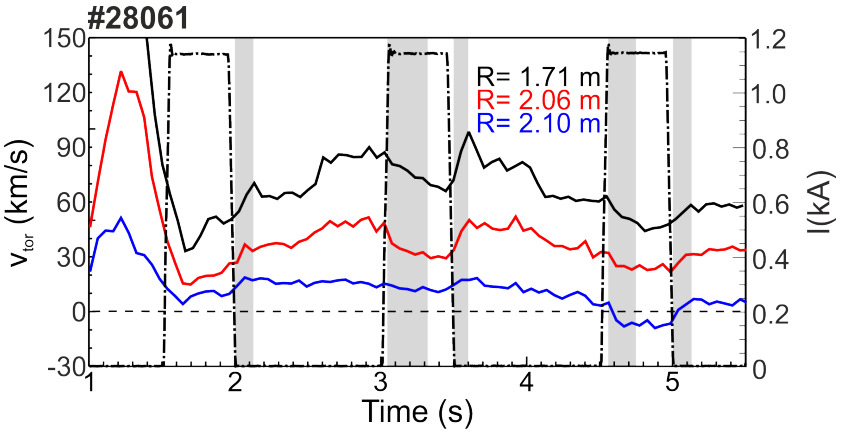

Figure 4.3: Temporal evolution of impurity toroidal rotation at different radial positions. Measurements from core and edge CXRS are shown. The rise and decay times are highlighted with gray shaded regions. The B-coils current is shown in a dashed line in the background for reference.

Finally, we focus on the response of the FILD signal. When the B-coils are turned on, the fast-ion losses rise to a level which can be several times higher than the NBI prompt loss level, see figure 4.4. The signal returns to the nominal prompt loss level when the B-coils are turned off. In addition, note that the base level is different in each NBI phase. This is because of different prompt losses associated to each NBI beam. The changes in the NBI prompt loss level are clearly seen in figure 4.4, where the continuous base level of FILD changes when the NBI source is switched. Because of a subtle variation of the integrated velocity-space signal for discharge #28059 (see figure 4.1(d)), the signal of one specific photomultiplier tube is shown for discharge #28059 to observe the change in the prompt loss level and the similarity of the patterns in response times for both discharges (as can be seen comparing figure 4.4 and 4.1(h)).

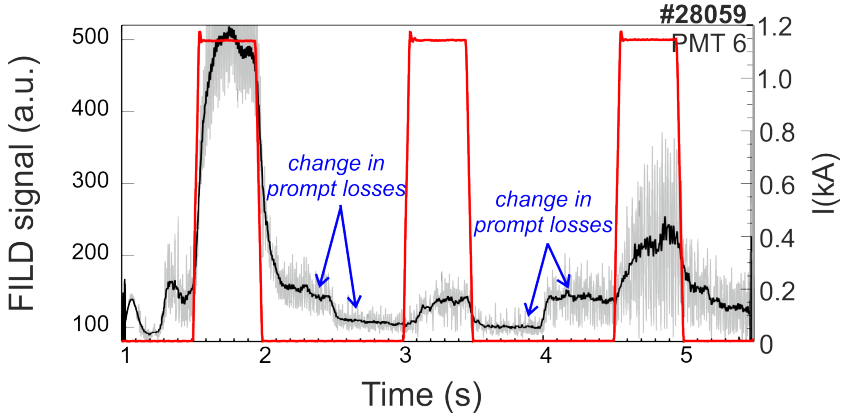

Figure 4.4: Temporal evolution one specific PMT of discharge #28059. The change in the base level is clearly seen and due to different prompt loss level.

A difference between rise and decay times of FILD signal has been previously observed in [6]. Two characteristic times in the temporal response to MPs are pointed out, the rise time around 10 ms and the decay time around 200 ms. It is important to notice that this pattern is observed for radial NBI beams (Q8 and Q5, phases 1 and 3) but not for tangential NBI beams (Q7, phase 2). Interestingly, the evolution of the FILD signal when using the tangential NBI shows a different pattern. In this case, the time scales are similar to the ones showed by rotation and the core density: the rise times ($\sim$ 200 ms) are slightly higher than the decay times ($\sim$ 100 ms). We observe the same response times in FILD signal for both discharges when we compare the pattern in figure 4.4 and figure 4.1(h). Figure 4.5 shows a zoom in of the first and second phase, which correspond to radial and tangential NBI beams, respectively. The core mode that develops in the first phase can be responsible for the rise in the FILD signal before the B-Coils are turned on. When the B-Coils are turned on and induce a large loss of fast-ions, they represent the

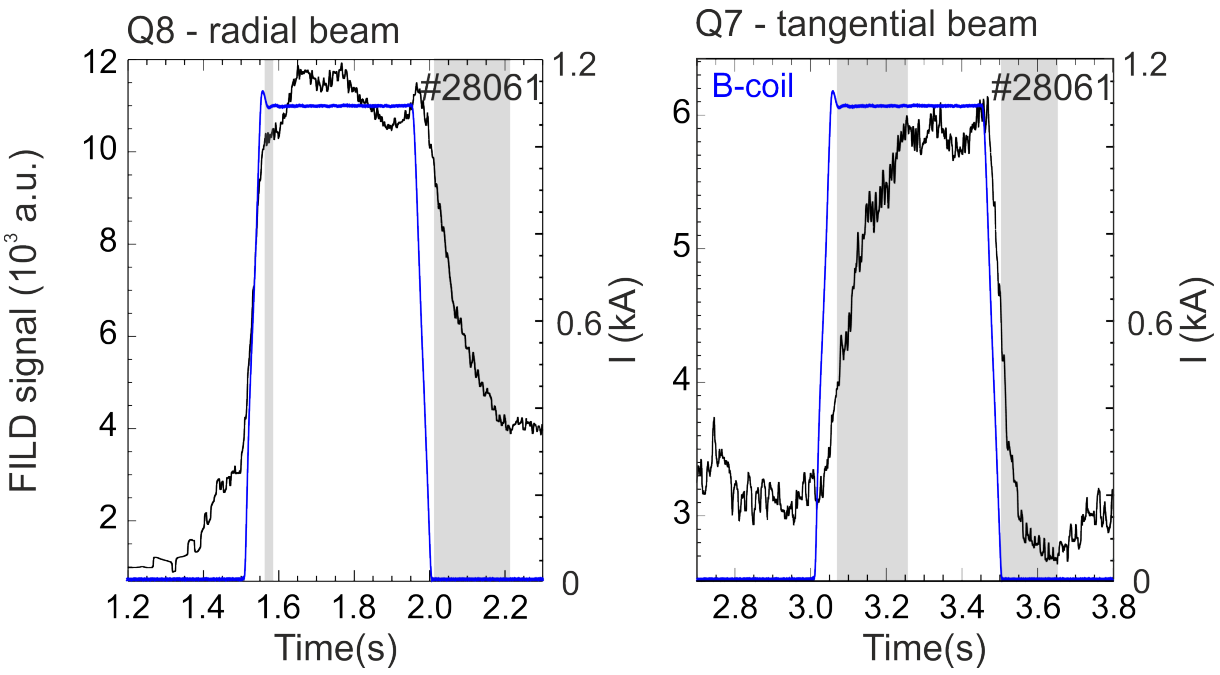

Figure 4.5: Temporal evolution of the FILD signal for radial and tangential injection. Characteristic times (highlighted in gray shade) are seen to be different depending on the injection geometry. The B-coils current is shown in blue in the background for reference.

dominant contribution to fast-ion losses. Thus, the rise time can be assumed to be due to the effect of magnetic perturbations. This is supported by the fact that the response times of fast-ion losses in the first phase are similar in discharge #28061 and #28059 (which has no core mode). The differences between rise and decay times are clear when changing the beams and suggest a different impact of MPs on losses of passing and trapped ions.

4.2 Rotation braking and acceleration

When the MPs are applied, a general rotation braking of the profile is observed and the evolution of the toroidal rotation is seen to be homogeneous in the plasma core. The CXRS diagnostics measure at fixed radial positions (see chapter 3.1.1). For a certain magnetic equilibrium, each radial position corresponds to a certain ρ_{pol}. The core and edge CXRS measurements are combined and mapped onto the magnetic equilibrium to obtain the profiles along ρ_{pol}. A polynomial fit has been performed to the rotation data for the whole profile. Example rotation profiles before and during the application of the MPs are shown in figure 4.6. In the plasma core, a rotation braking is observed. The evolution towards the plasma edge is more complicated. The rotation profile has been

observed to have a well structure at the edge in H-mode discharges [35]. Due to the experimental set-up of the discharges, the resolution in the edge is not sufficient to observe the well structure for all the time points within the MP phase. This is because of the specific plasma shape that is needed for the FILD measurements: the plasma is displaced further inside and does not allow for detailed rotation edge measurements.

An additional 2D fit, in time and ρ_{pol}, has been performed for the edge, in order to observe a more realistic evolution of the rotation in the ETB during the MP phases (for $\rho_{pol} \in [0.84, 1]$, see figure 4.7). The expected well shape is reconstructed (at $\rho_{pol} \approx [0.95, 1]$). When MPs are applied, an acceleration of $\sim$ -7 km/s is observed in the edge region, as the impurity rotation crosses zero and spins up in the counter-current direction. This means that at the plasma edge the impurities are accelerating in the opposite direction to the core. A dependence between pedestal collisionality and the minimum in toroidal rotation is seen in [36], [37]: below a collisionality threshold (around $\nu_i^* = 0.3$) the toroidal rotation minimum reaches negative values. This is in agreement with the fact that a low ion collisionality value, $\nu_i^* = 0.24$ at $\rho_{pol} = 0.95$, is reached in the last phase of the MPs in discharge #28061.

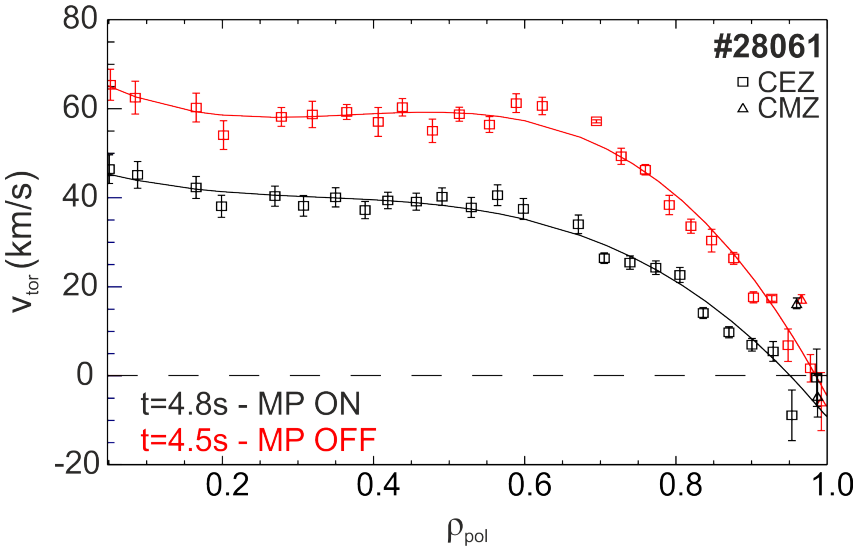

Figure 4.6: Radial profiles for impurity toroidal rotation during (t=4.8s in black) and before (t=4.5s in red) third MP phase for discharge #28061. Measured data with error bars are shown using different symbols for the core (CEZ represented with squares) and edge (CMZ represented with triangles) CXRS toroidal systems. The data is fitted to a polynomial at each time point.

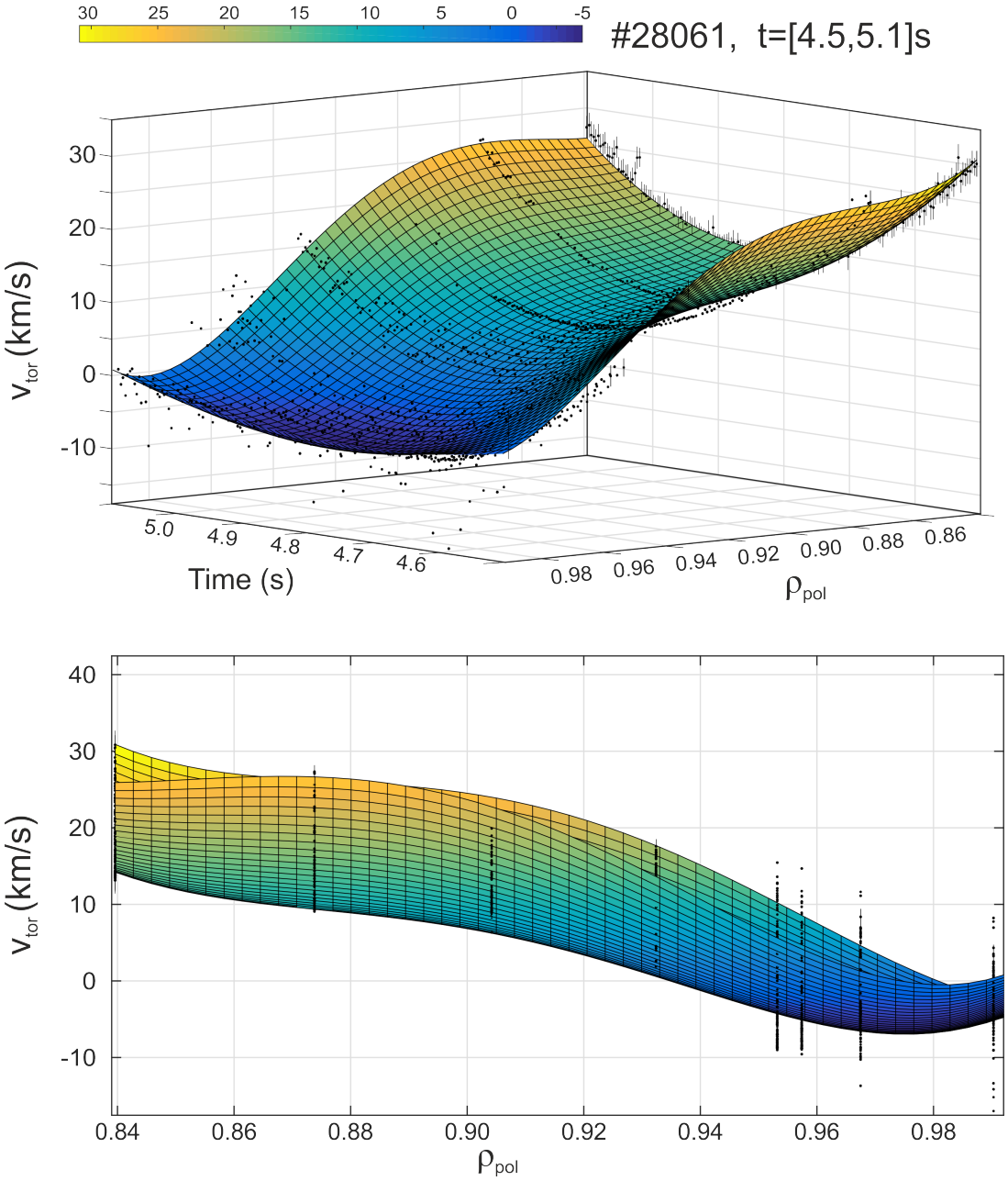

Figure 4.7: Separate surface fit for the edge toroidal rotation during a MP phase. The 2D fit in time and ρ_{pol} allows to observe the typical H-mode well structure in the toroidal rotation and its temporal evolution. The experimental data is represented with black dots. The uncertainties in the measurements are taken into account for the fit. Exemplary error bars are shown.

Chapter 5

Results

In the following chapter, the correlations between the signals are presented. The analysis of the signals needed for the calculation of correlation is presented in section 5.1. The temporal variation of the correlation coefficients is presented in section 5.2, and the effect of MPs on the correlation is pointed out. The dependence of the correlation on different parameters such as radial position and energy and pitch angle of fast-ions is presented in section 5.3.

5.1 Calculation of correlation

The signal processing and the correlation calculation was made by means of IDL routines. Prior to the calculation of the correlation, the data needed to be fitted. Due to the different time resolution of the diagnostics, a common time base is defined. The time resolution for the diagnostics is summarized in table 5.1.

CXRS core system	2.3 ms
CXRS edge system	3.5 ms
IDA	1 ms
FILD CCD Camera	20 ms

Table 5.1: Time resolution of the diagnostics used for the analysis in ms.

The common time base was defined according to the lowest time resolution signal, i.e. the CCD camera used for FILD. The signals were fitted in their time bases (so that the information of more precise diagnostics was not lost) and then interpolated from their

initial time base to the common one.

The rotation data was fitted using a 1D polynomial fit for the whole profile and an additional 2D fit for the detailed edge evolution (see section 4.2 and figures 4.6, 4.7). The radial density profiles provided by IDA are smooth and given as a function of ρ_{pol}. The density profiles were interpolated to the area base defined for CXRS to provide a common radial grid. In this manner, CXRS and IDA data could be correlated at different radial positions during the MP phases (note that here the radial position refers to the radial normalized coordinate ρ_{pol}).
The correlation is calculated by means of the linear Pearson coefficient ($C_{x,y}$), expressed as:

$$C_{x,y} = \frac{\sum_{i=1}^{N}(x_i \cdot y_i) - N\bar{x}\bar{y}}{\sqrt{(\sum_{i=1}^{N} x_i^2 - N\bar{x}^2)(\sum_{i=1}^{N} y_i^2 - N\bar{y}^2)}} \tag{5.1}$$

The IDL function *correlate* was used to calculate the correlation between the signals, which computes the linear Pearson correlation coefficient of the given signals. The correlation coefficient has values between 1 and -1. Values close to |1| indicate a strong coupled evolution, while values close to 0 indicate the evolution is decoupled. The sign determines if the evolution of the signals follows the same pattern i.e. when both rise/decay in time the sign of the correlation is positive, or an inverse pattern, i.e. when one signal is rising in time and the other is decaying the sign of the correlation is negative.
When the velocity is negative, the sign of the velocity is changed (i.e. the signal is mirrored) to study its correlation with the fast-ion losses and density. In this way, we can define positive/negative correlation in terms of acceleration/braking of the rotation, regardless of its sign.

5.2 Time evolution of the correlation

The correlation between the signals was calculated for the whole discharge to observe the impact of MPs on it. For this purpose, the correlation was calculated in overlapping time windows of 300 ms for the three NBI phases. The correlation was calculated for each time window and its value was assigned to the mean time of the time window. Here, the lag between two consequent time windows is 30 ms. The method is illustrated in figure 5.1 for clarity.

The correlation between the toroidal rotation and the fast-ion losses ($C_{v_{tor},FIL}$) integrated

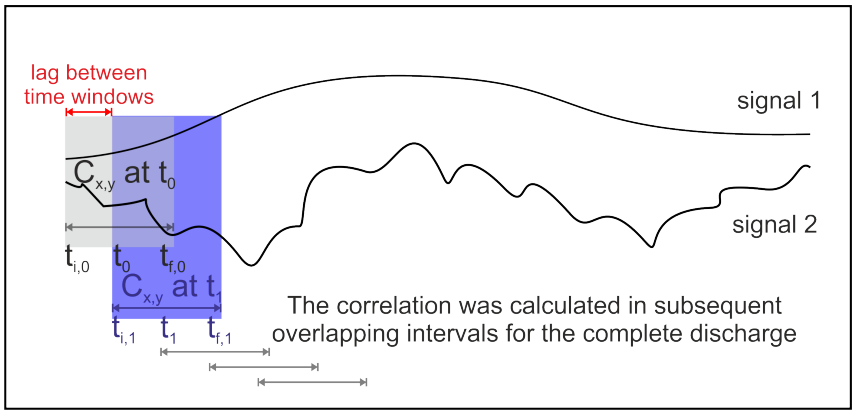

Figure 5.1: Method followed to analyse the variation in the correlation coefficient between a pair of signals as a function of time. Each time window is 300 ms long and the lag between two subsequent time windows is 30 ms. The time windows are overlapped.

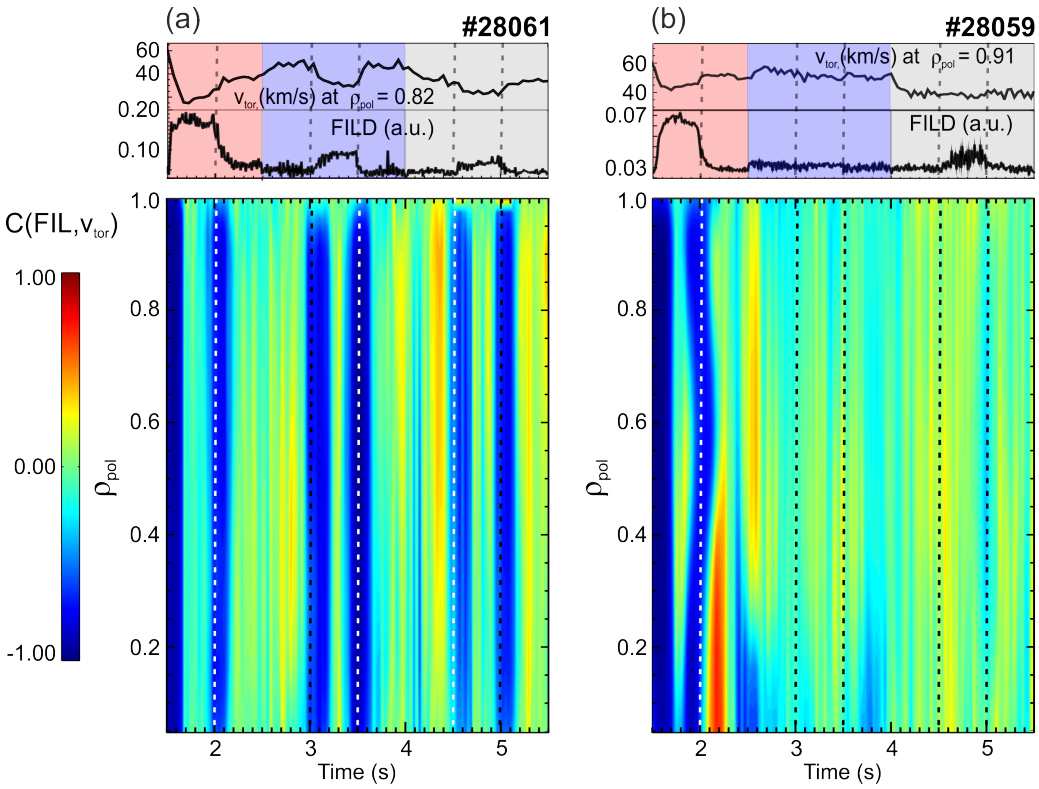

Figure 5.2: Correlation maps between fast-ion losses and toroidal rotation as a function of time and ρ_{pol} for discharges (a) #28061 and (b) #28059. B-coils turn ON/OFF is indicated with dashed lines. Exemplary rotation and fast-ion losses temporal evolution are given for reference. The changes in the NBI beams are indicated using different colours in the background (red, blue, gray).

over the whole velocity space (here, the signal from all the FILD photomultiplier tubes summed up is used) is presented in figures 5.2(a) and (b) for discharge #28061 and #28059, respectively. The dashed lines indicate when the B-coils are turned on and off. The correlation is clearly modulated by the MPs. When the B-coils are turned on, the fast-ion losses rise and the rotation decreases, while when they are switched off, the fast-ion losses decrease and the rotation rises, leading in both cases to negative correlation. When comparing figures 5.2 (a) and (b), we observe that the correlation modulation is stronger for discharge #28061 than for #28059, suggesting a stronger impact of the MPs on the correlation due to higher $I_{B-coils}/B_{tor}$ ratio for discharge #28061 (as discussed before, see figure 4.1 in chapter 4). The negative correlation structures extend mostly for all ρ_{pol}. The saturation stage within the MP phases shows up as intervals with low correlation values (coloured in green/turquoise/yellow) in between the high negative correlation structures. The same observation can be made when the B-Coils are switched off.

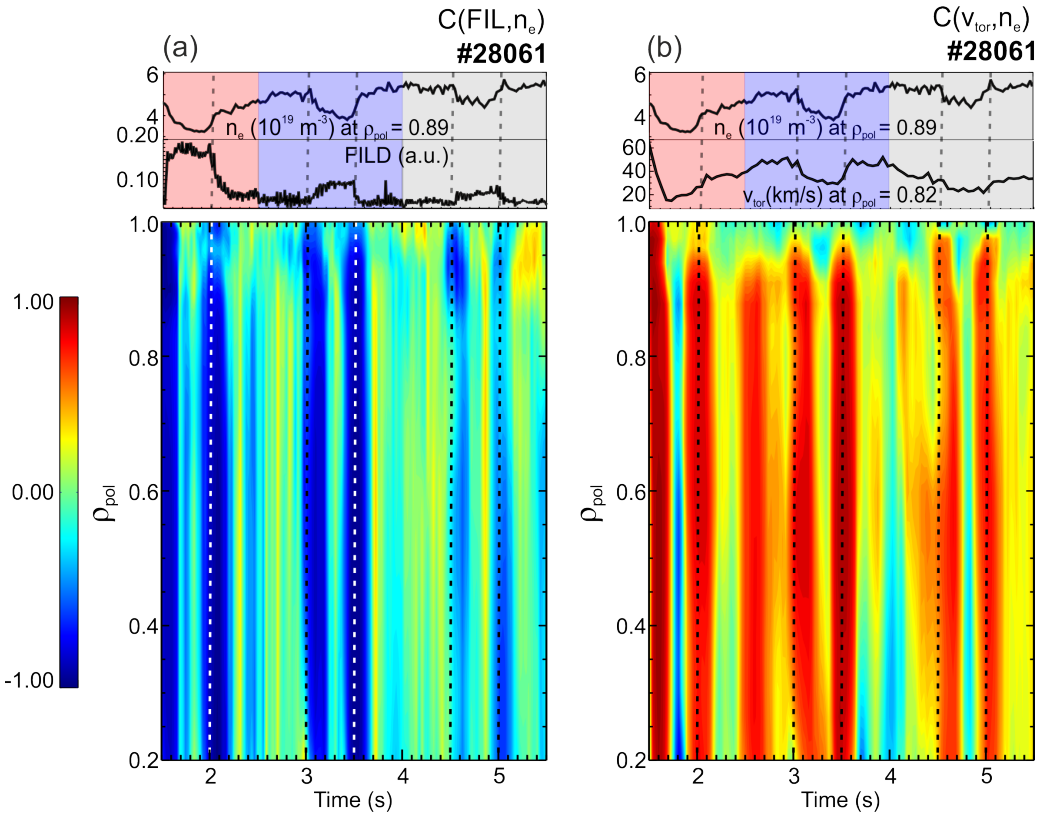

Figure 5.3: Correlation maps between (a) density and fast-ion losses and (b) density and toroidal rotation as a function of time and ρ_{pol} for discharge #28061. The switching ON/OFF time of the B-coils is indicated with dashed lines. Exemplary time traces of the signals are given for reference. The changes in the NBI beams are indicated using different colours in the background (red, blue, gray).

The correlation between density and fast-ion losses and density and rotation for discharge #28061 is shown in figures 5.3 (a) and (b), respectively. The results for discharge #28059 show similar structures (although not as intense as for discharge #28061) and are not presented for simplicity. Figure 5.3(b) shows additional correlation structures during the MP-off phases. These are induced by the changes in the NBI injection, which are indicated with different colours in the background of the signals time traces. The NBI injection influences the rotation, as momentum is transferred to the plasma.

The correlation structures are generally homogeneous for all radial positions, as density and rotation profiles undergo a general drop due to the MPs. Interestingly, it is possible to identify the faster response in the edge density due to the MPs. This effect is more obvious when the B-Coils are turned on, and can be clearly seen for instance in figure 5.3(a) at t=3 s: the change in correlation is simultaneous to the application of MPs at the edge, while a slightly slower response (a slight time delay in the correlation change) is seen in the core.

5.3 Dependencies of the correlation

In this section, the dependencies found for the correlation are presented. Figure 5.4 shows different frames of the FILD CCD camera before and during the application of magnetic perturbations. Similar frames showing differences in the fast-ion losses with and without magnetic perturbations for this discharge can be found in [6]. The regions with high emission indicate fast-ion losses for the values of pitch angle and energy assigned to the region. We observe that MPs produce losses of fast-ions that would be well confined in the absence of any perturbations (spots at pitch angle 35º and 55º at gyroradius around 4 and 3 cm, respectively, become visible when MPs are applied). The size reduction of the spot located around pitch angle 70º and gyroradius 3.5 cm suggests that losses for high pitch angle are mitigated due to MPs.

The correlation coefficient was calculated between the temporal evolution of density or rotation for all radial positions and the temporal evolution of fast-ion losses for different pitch angles and gyroradius during an MP phase. There, the signal of the FILD CCD camera has been used. The advantage of using the signal from the CCD camera is that it enables us to determine whether the whole velocity space of fast-ions follows a similar response to the MP. For this purpose, a grid with a resolution of 2 degrees in pitch angle

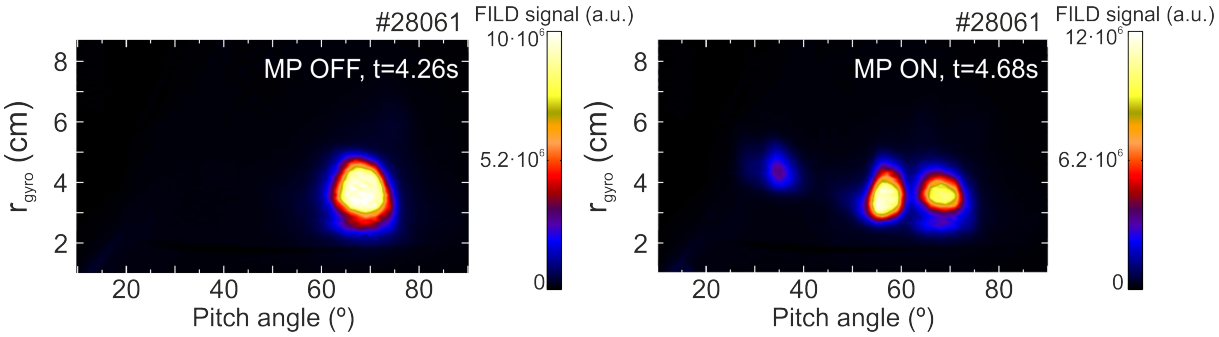

Figure 5.4: Frames of CCD camera before (left) and during (right) MPs phase with radial beam (Q5) for discharge #28061. Losses for pitch angle below (above) 60º are enhanced (mitigated) during MP phase.

and 0.5 cm in gyroradius has been defined. The intensity signal of pixels to which a range of pitch angle and gyroradius can be attributed, have been grouped together.

Figure 5.5(a)-(c) shows the temporal evolution of fast-ion losses for different pitch angles and gyroradius, density and rotation, respectively, for discharge #28061. The density and rotation time-traces are given at the same radial position ($\rho_{pol} = 0.967$). Figures 5.5(d) and (e) show the correlation maps for discharge #28061 as a function of pitch angle and gyroradius at a fixed radial position at which density/rotation are measured. Figure 5.5(f) and (g) show FILD CCD frames before and during the MP-phase to facilitate comparison of the fast-ion losses and the correlation patterns.

These correlation maps allow us to identify regions with mitigated/enhanced losses. By comparing figures 5.5(d) and (e) with (f) and (g), the regions with high absolute correlation values can be related with the regions in which fast-ion losses are produced. At this radial location, the density is decreasing: this means that the correlation is positive when fast-ion losses are mitigated (FILD signal decreases) and negative when losses are enhanced (FILD signal increases). The rotation reverses sign (from positive to negative) and an acceleration into the counter-current direction is observed: because of the opposite behaviour of density and rotation at this radial position, the correlation maps show similar patterns with opposite sign for the correlation coefficient. These correlation maps show similar structures when calculated for different radial locations. Note that towards the core, the density and rotation respond similarly to MPs (i.e. both decrease), so that deeper inside the plasma the pattern seen in the correlation map for rotation and density is similar to the one obtained for density at $\rho_{pol} = 0.967$. Deeper inside the plasma, a

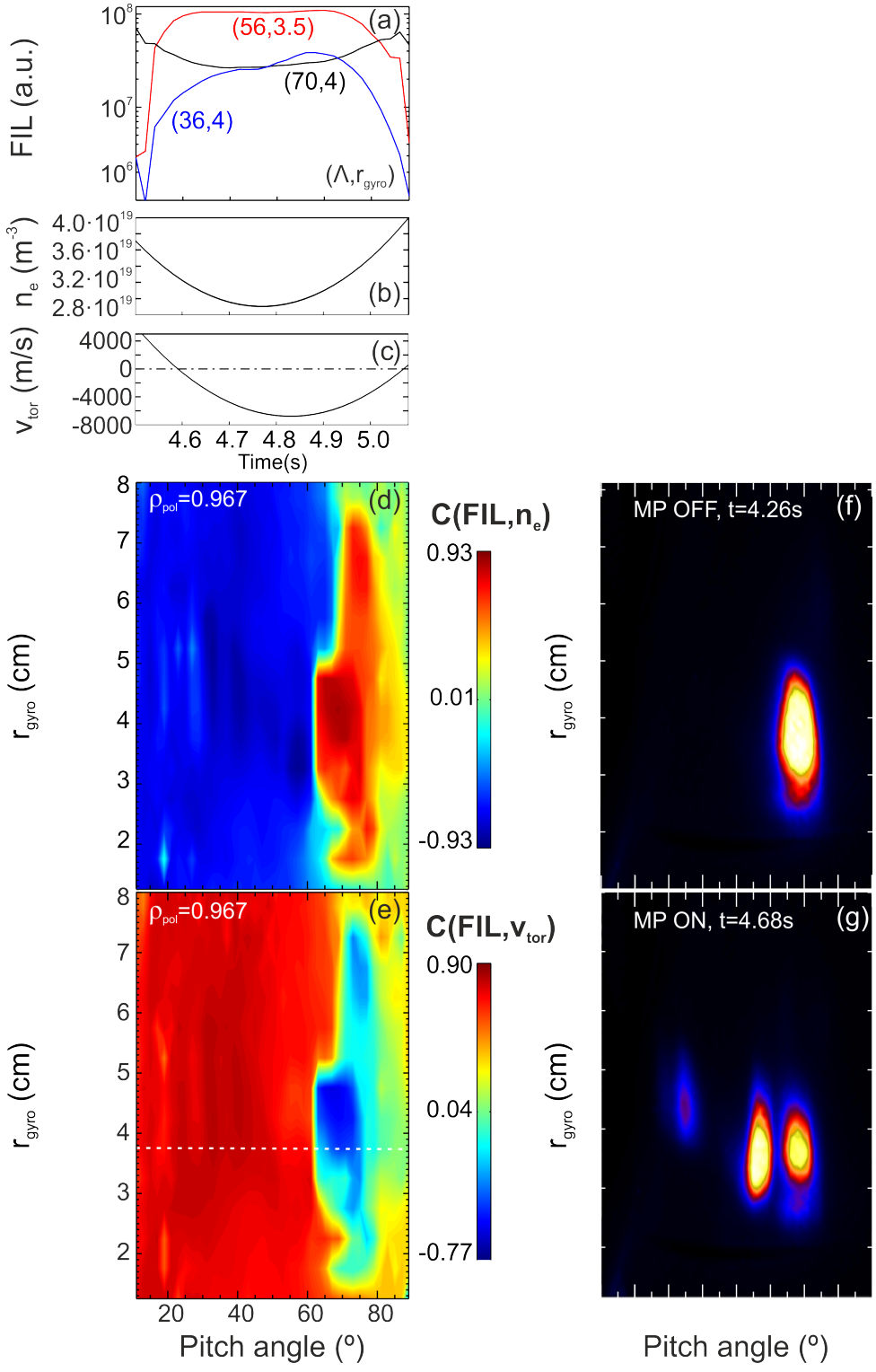

Figure 5.5: The temporal evolution of (a) fast-ion losses at different pairs (Λ, r_{gyro}), (b) density and (c) rotation during the third MP phase of discharge #28061. Contour plots show correlation maps between (d) density and fast-ion losses and (e) rotation and fast-ion losses at the edge ($\rho_{pol} = 0.967$) as a function of the pitch-angle (Λ) and gyroradius (r_{gyro}) of the fast-ions. FILD CCD frames (f) when MPs are not applied and (g) when MPs are applied are shown for reference.

rotation braking is observed and the correlation between density and rotation is strong and positive (both decrease), while at this specific radial position the correlation between rotation and density is -0.73 (as density decreases and rotation increases).

Interestingly, there is an abrupt change in the correlation coefficient for a given pitch angle (see figures 5.5)(d) and (e). Around pitch angle 60-65º and gyroradius 3.5-4 cm, the correlation coefficient changes from -0.90 to +0.90 for the correlation between fast-ion losses and density and from +0.75 to -0.70 for the correlation between fast-ion losses and rotation. This can be identified as the trapped/passing boundary, suggesting the topology of the orbit strongly influences the pattern of losses. In this case, MPs enhance the losses of passing particles.

A similar pattern is seen for the same phase (third phase, radial NBI injection geometry) in discharge #28059. This pattern is not observed for all phases. For instance, for the second phase in discharge #28059 an opposite effect is seen, as losses are mitigated for pitch angles around [40,50]º and enhanced for pitch angles [60,70]º (these figures are not shown). This can be attributed to the change in the NBI injection geometry that leads to different fast-ion populations. In fact, it leads to opposite behaviour of what is shown in figure 5.5.

Figures 5.6(a) and (b) show changes in the correlation between toroidal rotation and fast-ion losses as a function of pitch angle and radial position for a fixed gyroradius (a cut-through along the white dashed line indicated in figure 5.5(e), now varying the radial coordinate given by ρ_{pol}). The difference between the figures 5.6(a) and (b) is the ρ_{pol} ranges. Figure 5.6(a) shows the correlation map for the whole rotation radial profile (the rotation profiles have been fitted by means of the polynomial fit shown in figure 4.6). In figure 5.6(b) the focus is placed on the plasma edge ($\rho_{pol} > 0.85$) and this correlation map has been obtained using a dedicated fit for the edge rotation (shown in figure 4.7). The correlations are calculated for the time evolution of fast-ion losses with a gyroradius ranging from 3.5 to 4 cm, corresponding to an energy range from 88 to 115 keV (the first energy component of the NBI injected fast-ions is 93 keV). Figure 5.6(a) shows that the correlation structures extend for all radial positions and are more intense towards the edge (from ρ_{pol} around 0.8 to 0.98). This corresponds to the region where fast-ions are born and suggests that the largest effects of fast-ions losses on rotation are at the edge, in agreement with the fact that fast-ions striking on FILD are edge particles exploring

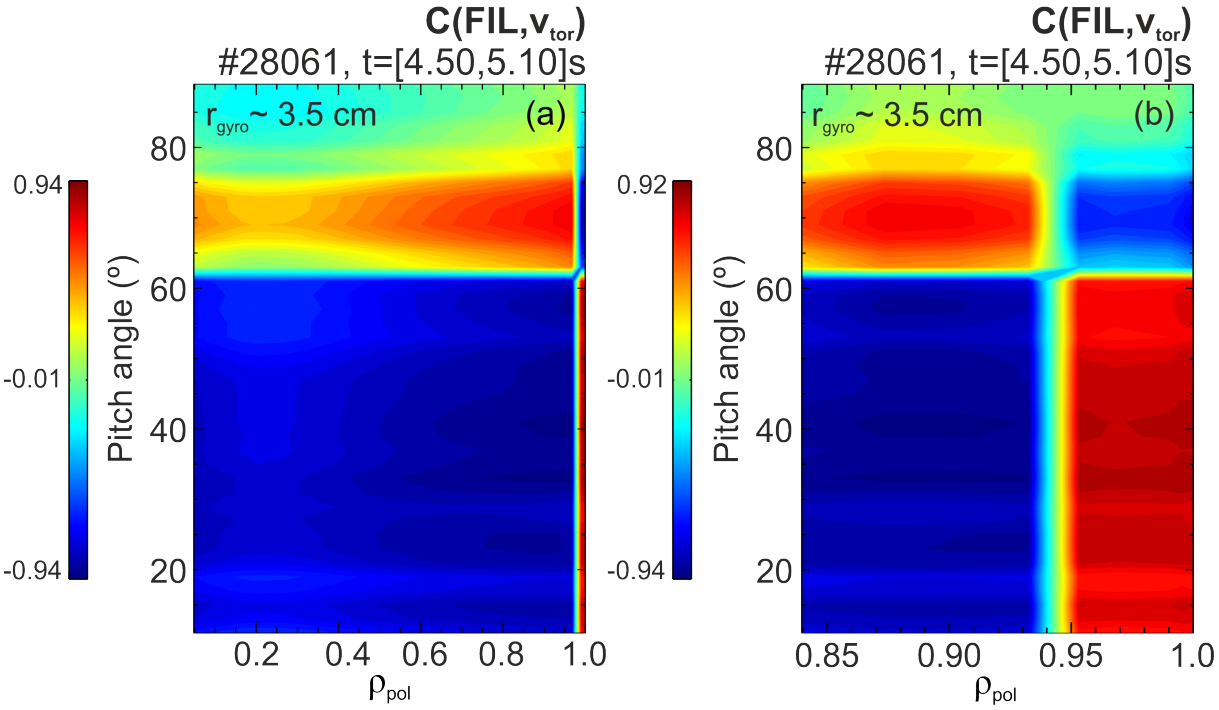

Figure 5.6: Correlation maps between rotation and fast-ion losses as a function of radial position (ρ_{pol}) and pitch angle at constant fast-ion gyroradius for third MP phase of discharge #28061. The correlation is seen to be stronger towards the edge. Just inside the separatrix, a change in correlation sign is due to the reversal of the rotation and the acceleration of impurities in counter-current direction. (a) Correlation map from the plasma core up to the separatrix. (b) Dedicated correlation map for the edge (obtained using a dedicated profile fit for the plasma edge rotation).

the pedestal, as presented in figure 2.6(b). Towards the separatrix, an abrupt change in the correlation is seen. This change in the correlation sign is due to the acceleration of impurity rotation at the edge, in contrast with the rotation braking observed deeper inside. The change in the correlation sign towards the separatrix ($\rho_{pol} = 1$) is seen in both figures 5.6(a) and (b), where (b) presents more accurately the behaviour of the plasma edge, as it has been obtained using a dedicated fit for this region.

Chapter 6

Summary and discussion

The results obtained in this thesis contribute to the understanding of the impact of magnetic perturbations on different parameters. A correlation study was performed to analyse the coupled evolution of the impurity toroidal rotation, fast-ion losses and plasma density. A detailed analysis of two low collisionality ASDEX Upgrade H-mode discharges was performed and yields information about the interdependencies between the parameters.

The density, toroidal impurity rotation and fast-ion losses show strong modulation due to the externally applied magnetic perturbations (MPs). During the application of the perturbations, the phenomenon of density pump-out is observed. Fast-ion losses are enhanced or mitigated with a strong dependence on the topology of the orbit (which depends on their pitch angle). Overall, a braking in the impurity toroidal rotation is observed during the MP phases. For a certain phase, which presents lowest ion collisionality, an acceleration of the impurities in the counter-current direction is seen at the plasma edge, consistent with the observation that the impurity toroidal rotation is negative below a certain collisionality threshold. The response of the parameters to the MPs leads to correlation patterns that strongly depend on (1) the characteristics of the fast-ion population subject to losses and (2) the radial position at which rotation and density are measured.

The correlation is seen to become more intense towards the plasma edge, in agreement with the observation that the lost fast-ions are born at the edge and thus can have a stronger impact on rotation in this region. The observation of an abrupt change in the

correlation due to a variation in pitch angle suggests the effect of the accumulation of resonances in the trapped/passing boundary, which can affect the confinement of fast-ions. This result is in line with previous observations of the existence of an edge resonant transport layer [21], [38].

Appendix A Uncertainty estimation

The impact of the uncertainties on the calculation of the correlation is evaluated in this appendix. For this purpose, the uncertainty of the correlation coefficient has been calculated using Gaussian error propagation and additionally estimated by two methods. The expression for the linear Pearson coefficient ($C_{x,y}$) is given in equation (5.1). Its uncertainty ($\Delta C_{x,y}$) can be calculated as:

$$\Delta C_{x,y}^2 = \left(\frac{dC_{x,y}}{dx_i}\right)^2 \cdot \Delta x_i^2 + \left(\frac{dC_{x,y}}{dy_i}\right)^2 \cdot \Delta y_i^2, \tag{6.1}$$

which gives:

$$\begin{aligned}
\Delta C_{x,y} \quad = \quad & \frac{1}{\sqrt{(\sum_i x_i^2 - N\bar{x}^2)(\sum_i y_i^2 - N\bar{y}^2)}} \cdot \\
& \left\{ \sum_i \left[y_i - \bar{y} - \frac{(\sum_i (x_i y_i) - N\bar{x}\bar{y})(x_i - \bar{x})}{\sum_i x_i^2 - N\bar{x}^2} \right]^2 \cdot \Delta x_i^2 \quad + \right. \\
& \left. \sum_i \left[x_i - \bar{x} - \frac{(\sum_i (x_i y_i) - N\bar{x}\bar{y})(y_i - \bar{y})}{\sum_i y_i^2 - N\bar{y}^2} \right]^2 \cdot \Delta y_i^2 \right\}^{1/2}
\end{aligned}$$

In figure 6.1(a) the correlation coefficient and (b) its uncertainty following Gaussian error propagation are presented. Note that for the uncertainty the Z-axis goes from 0 to 1. By comparing both figures, one can note that the most narrow semi-confidence intervals are given for the regions with high correlation, being of the order of 0.10 in these regions. The uncertainty for most of the map is under 0.30, and only reaches high values in a small region which corresponds to regions where the fast-ion loss signal is very low.

Two additional methods evaluate to the uncertainty in the correlation coefficient were used. The first method is based on the estimation of the confidence intervals for the Pearson correlation coefficient using the traditional method (Fisher's transformation). The second method evaluates the impact of the uncertainty in the measurements on the value of the correlation coefficient and its deviation by means of a simulation based on a random number generator. The values for the correlation coefficient obtained following the two methods are presented in figure 6.2, while their deviations are presented in figure 6.3.

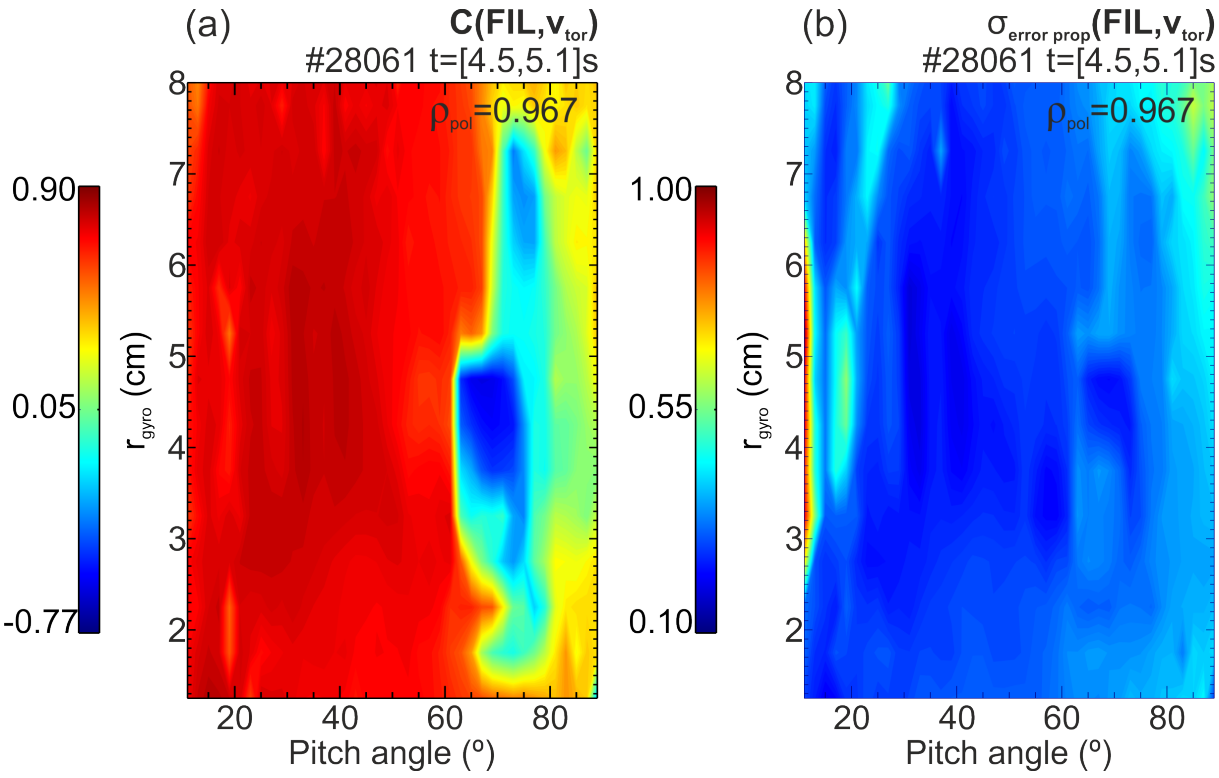

Figure 6.1: (a) Pearson correlation coefficient between fast-ion losses and rotation at the specific radial position ($\rho_{pol} = 0.967$) and (b) its uncertainty calculated by Gaussian error propagation.

For the first method, the experimental data are fitted taking into account their uncertainties (as described in chapters 4.2 and 5.1) and the correlation coefficient was calculated using these fitted signals (C_{Fisher}). This is the procedure that has been followed in this thesis (note figure 6.1(a), figure 6.2(a) and figure 5.5(e) are the same correlation map). The confidence interval of the correlation has been estimated using the Fisher transformation and it depends on the value of the Pearson coefficient itself and the sample size. The confidence interval has been calculated for a confidence level of 95% ($\sigma_{Fisher,95\%}$). As the interval is asymmetric, the value of the limit that drives the correlation towards zero is presented in figure 6.3(a). It is interesting to note that the broader intervals are given for regions that present low values for the correlation coefficient and viceversa, as can be deduced comparing figures 6.2(a) and 6.3(a). The narrower the intervals, the more significant the correlation coefficient. This confirms the significance of the correlation coefficient in the cases of interest, which are the ones that have high correlation coefficient.

For the second estimation, the experimental measurements have been fitted and afterwards randomly altered taking into account their experimental uncertainties. For this

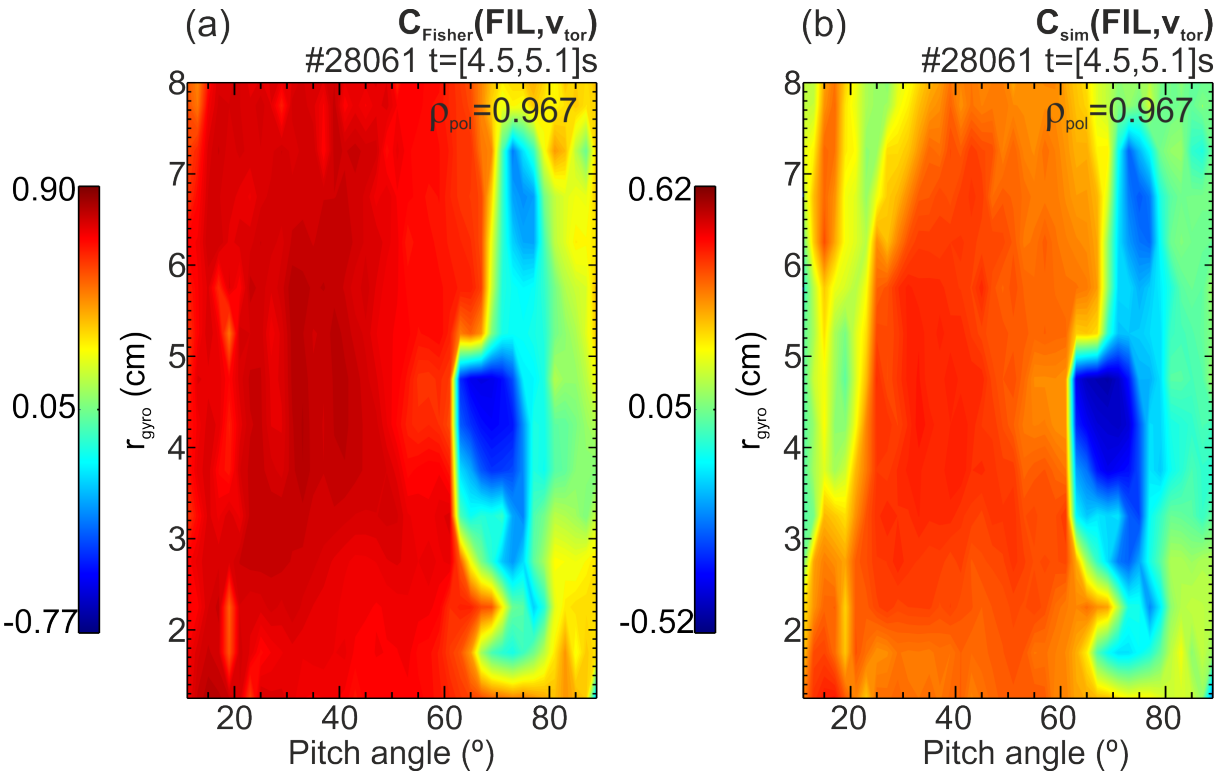

Figure 6.2: Pearson correlation coefficient calculated by means of (a) the first method and (b) second method.

purpose, a pair of random numbers have been generated to determine the sign and percentage of the experimental uncertainty to be added. In this manner, a random percentage of the uncertainty is added to the measurement, giving an altered signal. The correlation between the pair of altered signals has been calculated, and this procedure has been repeated over a hundred times for each pair of signals, leading to a sample of 100 values for the correlation coefficient. The correlation coefficient and its confidence interval has been calculated by means of the average (C_{sim}, figure 6.2(b)) and standard deviation (σ_{sim}, figure 6.3(b)) of the sample. Note that the semi-confidence interval shown in figure 6.3(b) is actually 1.96 times the standard deviation of the sample, an thus represents the same confidence level (95%) as the one calculated by means of the first method.

The second method, which takes into account the uncertainty in the measurements, leads to lower absolute correlation coefficients. However, the correlation pattern holds for the whole map and confirms the validity of the correlation analysis at this radial location. The uncertainties in the correlation associated to the statistical nature of the correlation ($\sigma_{Fisher,95\%,}$) and to the uncertainties in the measurements ($\sigma_{sim,}$) are comparable. When

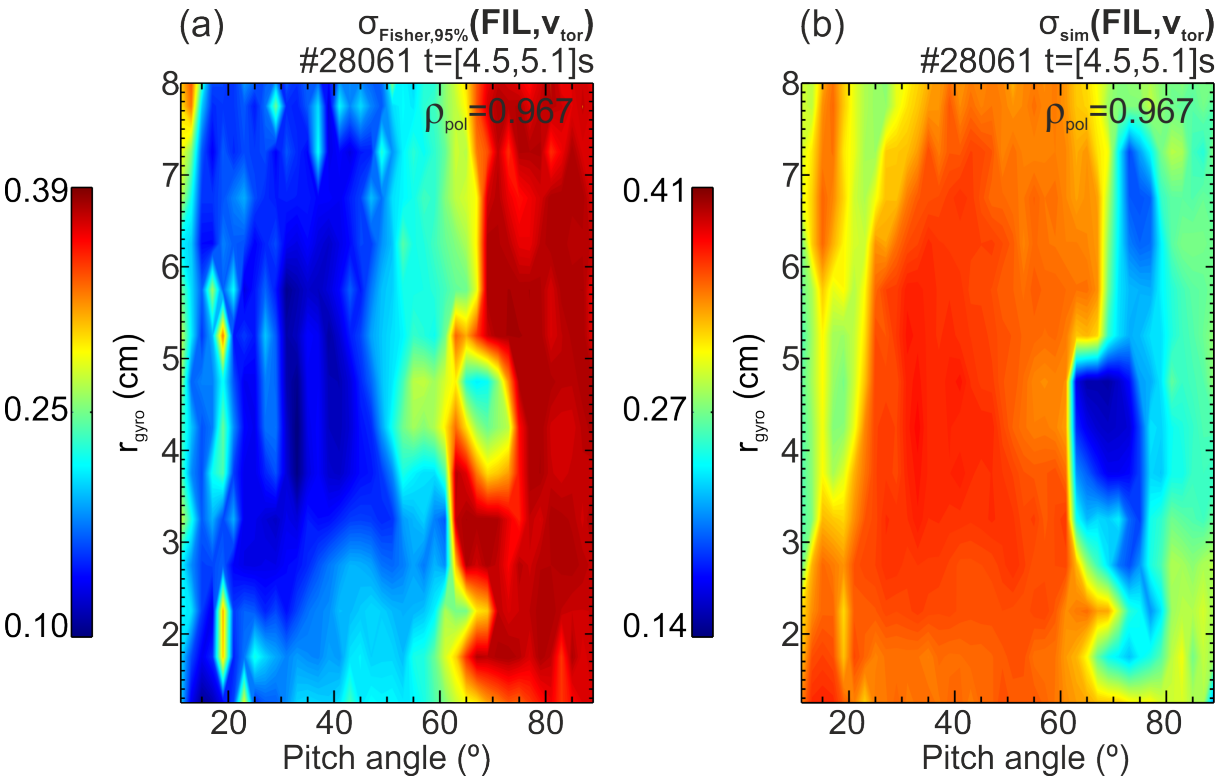

Figure 6.3: Value of a semi-confidence interval of the correlation coefficient calculated using (a) Fisher transformation with 95% of confidence level and (b) standard deviation of C_{sim}.

the second method is applied to the data measured in the core (outside of the separatrix), the correlation patterns between fast-ion losses and density (rotation) are not visible due to the large uncertainties in the measurements, as one would expect.

The comparison of the results obtained by the two methods allows to validate the correlation analysis, as the same pattern for the correlation coefficient is observed.

Acknowledgements

I first want to thank Dr. Eleonora Viezzer, for all her patience and dedication. Thank you, gracias, Danke. You took me by the hand to the world of fusion energy, and gave me a great opportunity. I have been incredibly fortunate to have you as my supervisor.

I also want to thank Manolo and Joaquín, who closely followed this thesis. Thanks to the whole PSFT group for your support and kindness during the last months.

I have been very lucky to share this experience with Diego. If having you as a classmate during the master was great, I do not have words to express how it was to have you as a friend. I take advantage to also thank Damián and Tere for the many hours of work and laughs in Sevilla, and Javi and Anton who made nicer my stay in Garching. Many thanks to my friends in Murcia and Valencia who always cheered me up.

Last but not least, I want to thank my family. Million thanks for your unconditional support. Thanks for being always by and on my side!

Bibliography

[1] J. Wesson. *Tokamaks.* 3^{rd} edition, ISBN 0 19 8509227, Oxford University Press, Oxford, 2004.

[2] University of Wisconsin (Madison). *Inertial Electrostatic Confinement Fusion.* URL http://iec.neep.wisc.edu/images/crossSections.jpg/, 2014.

[3] EUROFUSION. *European Consortium for the Development of Fusion Energy.* URL http://www.euro-fusion.org/, 2017.

[4] F. Chen. *Introduction to plasma physics and controlled fusion.* 2^{nd} edition, Plenum press, New York and London.

[5] M.W. Jakubowski *et al.* 25^{th} *IAEA Int. Conf. on Fusion Energy*, EX/P3-47, 2014.

[6] M. Garcia-Munoz *et al. Plasma Phys. Control. Fusion*, 55:124014, 2013.

[7] M. Garcia-Munoz *et al. Nucl. Fusion*, 53:123008, 2013.

[8] F. Wagner *et al. Physical Review Letters*, 49(19):1408, 1982.

[9] M. Keilhacker *et al. Plasma Phys. Control. Fusion*, 29(10A):1401–1413, 1987.

[10] E. Viezzer. *Radial electric field studies in the plasma edge of ASDEX Upgrade.* PhD thesis at Ludwig-Maximilians-Universität, Munich, 2012.

[11] U. Stroth *et al. Plasma Phys. Control. Fusion*, 53:024006, 2011.

[12] E. Viezzer *et al. Rev. Sci. Instrum.*, 83:103501, 2012.

[13] J.W. Connor *et al. Phys. Plasmas*, 5:2687, 1998.

[14] P.B. Snyder *et al. Phys. Plasmas*, 9:2037, 2002.

[15] W.A. Suttrop *et al.* 43^{rd} *EPS Conference on Plasma Physics*, 15380.

[16] T.C. Hender *et al. Nucl. Fusion*, 32:2091, 1992.

[17] T.E. Evans *et al. Phys. Rev. Lett.*, 92:235003, 2004.

[18] W. A. Suttrop *et al. Phys. Rev. Lett.*, 106:225004, 2011.

[19] E. Viezzer *et al. Nucl. Fusion*, 53:053005, 2013.

[20] G. D. Conway *et al. Plasma Phys. Control. Fusion*, 57:014035, 2015.

[21] L. Sanchis *et al.* 43^{rd} *EPS Conference on Plasma Physics*, P1.056, 2016.

[22] R.J. Fonck *et al. Physics Review A*, 29:6, 1984.

[23] M. Cavedon *et al. Review of Scientific Instruments*, 88(4):043103, 2017.

[24] D.S. Darrow *et al. Rev. Sci. instrum.*, 66:476, 1995.

[25] M. Garcia-Munoz *et al. Rev. Sci. instrum.*, 80:053503, 2009.

[26] M. Garcia-Munoz *et al. Nucl. Fusion*, 47:L10–L15, 2007.

[27] J. Galdon Quiroga. *Development of synthetic fast ion loss detector for fusion devices.* Master thesis at Universidad de Sevilla, Sevilla, 2014.

[28] R. Fischer *et al. Fus. Sci. Technol.*, 58(675), 2010.

[29] J. Schweinzer *et al. Plasma Physics and Controlled Fusion*, 34(1173), 1992.

[30] A. Mlynek *et al. Rev. Sci. Instrum.*, 81(033507), 2010.

[31] W.A. Suttrop *et al. Fusion Eng. and Design*, 84:290, 2009.

[32] Y. Liu *et al. Plasma Phys. Control. Fusion*, 58:114005, 2016.

[33] B. Streibl *et al. Fusion Science and Technology*, 44:578–592, 2003.

[34] N. Leuthold *et al. Plasma Phys. Control. Fusion*, 59:055004, 2017.

[35] T. Pütterich *et al. Physical Review Letters*, 102:025001, 2009.

[36] E. Viezzer *et al. Nucl. Fusion*, 53:123002, 2015.

[37] D.J. Cruz Zabala. *Characterization of the ion pedestal in low and high collisionality plasmas.* Master thesis at Universidad de Sevilla, Sevilla, 2017.

[38] M. Garcia-Munoz *et al.* 26^{th} *IAEA Fusion Energy Conference*, EX/6-1, 2016.